POLITECNICO DI TORINO

Master's Degree in Aerospace Engineering

Master's Degree Thesis

Manufacturing and validation of 3D printed space structures via multiaxial testing

Supervisors
Prof. Enrico ZAPPINO
Dr. Eng. Alberto GARCIA DE MIGUEL
Eng. Ruben ARAUJO

Candidate
Samuele MONTESION

December 2024

Summary

Since its first apperance in 1999, the CubeSat standard has made access to space more affordable and easier for small realities such as universities and research institutions. The cost of a CubeSat already dropped a lot thanks to the availability of Off The Shelf components, but the structure is still an expensive part if you want it customized. A viable option to reduce its costs and increase customization is to produce it using Additive Manufacturing methods.

Following this introduction, in the first part of the thesis, the author has designed two different 1U CubeSat structures that have then been manufactured using the Fused deposition modelling (FDM) process. In particular the structures have been printed using PEEK, a material that can and has already been used in space. The two structures differ in approach, one follows a more classic design similar to the ones already in use in the industry and the other is designed trying to use in the best way possible the advantages that Additive Manufacturing offers.

Rigorous testing is crucial for ensuring space structures can withstand the harsh launch environment. One of the most critical factors to consider is the vibration experienced during launch. The forces acting on the launch vehicle and satellite are predominantly multi-directional and random in nature. However, traditional vibration testing methods typically rely on single-axis excitation, failing to fully capture the complex vibration modes of the satellite. In contrast, Multi-Input-Multi-Output (MIMO) testing approaches are capable of more accurately replicating the realistic multi-dimensional vibration environment encountered during launch. This enables a more comprehensive evaluation of the satellite's structural integrity and failure modes, leading to improved design and qualification for the actual launch conditions.

In the second part of the thesis the author focused on creating an environment as similar to reality as possible using a 4-DOF shaker that allows the object to be subjected not only to all three translations but also one rotation all at the same time. This was done in primus by using the same profile, in terms of excitation, that is already used for the single axis testing and using it for all three translations. Then the author tackled another problem: the use of a CLA-like (Coupled Load Analysis) environment as target. The problem in recreating this environment on a multi-axial shaker is given by the difficulty in making the table recreate that environment, in particular the rotations, using only linear accelerometers. This thesis gives a procedure to solve this problem and that can be used in other situations. In general the work aims to provide a complete into the design, manufacturing and advanced structural testing of an AM-built CubeSat.

Acknowledgements

First and foremost, I would like to express my deepest gratitude to my professor at Politecnico di Torino and my two supervisors at Siemens. Their unwavering support, insightful guidance, and valuable feedback have been instrumental from the very first day of this research project to its conclusion. Their mentorship has not only enriched my academic journey but also shaped my professional growth.

I am immensely grateful to my friends in Turin, who stood by me during these two intense years of the master's program. Their companionship and encouragement provided much-needed balance during challenging times. Equally, I want to thank the friends I made in Belgium, who welcomed me warmly and fostered an environment where I could thrive both professionally and personally. Their camaraderie turned this experience into an unforgettable chapter of my life.

A heartfelt thanks goes to my girlfriend, who has been my constant supporter since the moment I decided to embark on this journey at PoliTo six years ago. Her unwavering belief in me, through every high and low, has been a constant source of strength.

Lastly, but most importantly, I want to express my profound appreciation for my family. Their unconditional love and support have been the cornerstone of my journey. Without their encouragement and assistance, completing this thesis—and reaching this milestone—would not have been possible. To them, I owe the deepest gratitude for being my foundation and my greatest inspiration.

Table of Contents

List of Tables

List of Figures

Chapter 1

Introduction

1.1 CubeSats

CubeSats are a class of small satellites, used primarily for research purpose, with a standardized dimension of 10x10x10 cm, weight of no more than 2 Kg per unit and typically use Commercial Off The Shelf (COTS) components[1]. The project started in 1999 as a collaboration between the California Polytechnic State University and Stanford University's Space System Development Laboratory after which they published the CubeSat Design Specification document where they specify the basic requirements in terms of design, manufacture and testing of the satellite.
The purpose of the project and the standard was and it still is to allow smaller realities, like universities and research institutions, to have access to space.

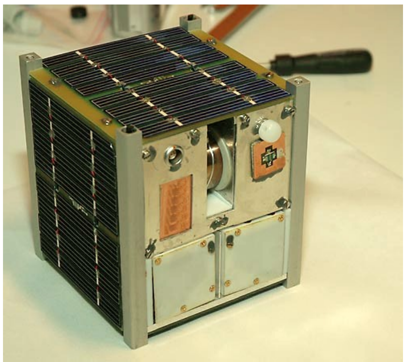

Figure 1.1: Norvegian CubeSat nCube-2 1U[2]

CubeSats, in the form of 1U to 6U, being this small, are never the primary payload on the spacecraft, in fact, they use what is called a Piggy Back kind of transport to go to orbit. They are put in a more external part of the spacecraft closer to the nozzle of the last stage and from there they are deployed into orbit using a dispenser, which is also standardized, the P-POD (Poly-PicoSatellite Orbital Deployers).[4]

Figure 1.2: ISIPOD CubeSat Deployer 3U[3]

Bigger Cubesat such as 12U or 16U can become the primary payload of the spacecraft if in good quantity. The transfer type that is used in this case in a Rideshare like the one that was used for the inaugural flight of the Ariane 6.

1.1.1 CubeSat Structures State of the art

One of the most important subsystem of the satellites in general, is the structure. The design of the CubeSat allows it to be scalable from 1U to 16U.
Structures can be Monocoque constructions or Modular Frame designs. The second one allows more internal flexibility while still ensuring external requirements. The third option is a custom machined structure that enable grater flexibility in mission specific payload design.
The materials used for these structures must have the same coefficient of thermal expansion as the deployer to prevent jamming. The only materials used as of this moment are: Aluminium 7075, 6061, 6082, 5005 and 5052. Other materials can be used but the launch provider and the dispenser manufacturer must agree.
The average weight of a 1U Aluminum CubeSat structure is 0.118 Kg [4]. In the figure below we can find an example of COTS structure for a 1U CubeSat.

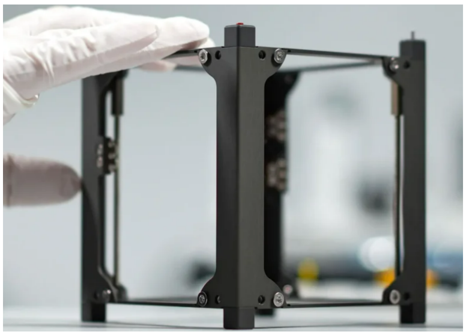

Figure 1.3: 1U CubeSat structure by EnduroSat in aluminum 6082[5]

1.2 Additive manufacturing

With the term Additive manufacturing we are referring to a broad range of production methods that fabricate products layer by layer. The more widely used AM processes are: fused deposition modelling (FDM), stereolithography (SLA), selective laser melting (SLM), selective laser sintering (SLS) and electron beam melting (EBM).[6]
Additive manufacturing in general brings a lot of advantages to the table:

- Increased design freedom
- Lighter structures made possible by creating optimized design that put material only where it's needed.
- Several parts can be built in one printing session or even in one design
- Less raw material consumption up to 25 times less then machining production.
- No tools needed
- Short production cycle time, even for more complex parts
- Small series production a lot cheaper then using traditional processes

To produce an additive manufactured component the process is simple. It all starts from a 3D computer aided design (CAD) model where the geometry is defined. It then has to be converted into an STL (stereolithographic file) model where all the surfaces of the geometry are represented with a finite number of adjoining triangular facets. Afterwards the STL file can be put into a slicer software that allows to divide the part in a number of layer that is a function of the characteristics of the machine and process used. The slicer software can be proprietary, which gives more option for that exact machine, or open source. The slicing process introduces geometric error known as stair-step effect which becomes significant as the inclination angle of the part becomes more acute or as the thickness of the layer increases. In the slicer it is also possible to see where the supports are needed. These were the steps common to every additive manufacturing process, after that every process have different parameters and also different steps, like some of them that require post processing.[6]

1.2.1 Fused Deposition Modelling

Fused deposition modelling is an AM process where a filament is fed to the head of the printer where it is liquefied. The liquid is then pushed through a nozzle and applied on the platform or the previous layer. The nozzle is an important part of the machine because it determines the shape and size of the extruded filament. A larger nozzle will enable material to flow more rapidly but it will resolve in a part with lower precision. It also determines the minimum size of the feature that can be created.
The mechanism of the fusion in FDM process depends upon time taken for solidification. The 2 layers, the new one and the last one, interact with each other while one of them is in a molten condition. This create a bond between them.
In the most common type of machine for this process, the head moves along the XY plane and the platform along the Z axis. Each time a layer is finished the platform moves down by one layer thickness and then start the new layer. Other possible combination of movement are available, for example, in same cases is only the head that moves in every direction.
The fact that this process is widely used in different sectors and at different level allows the constant development and improvements in every aspect of the process.

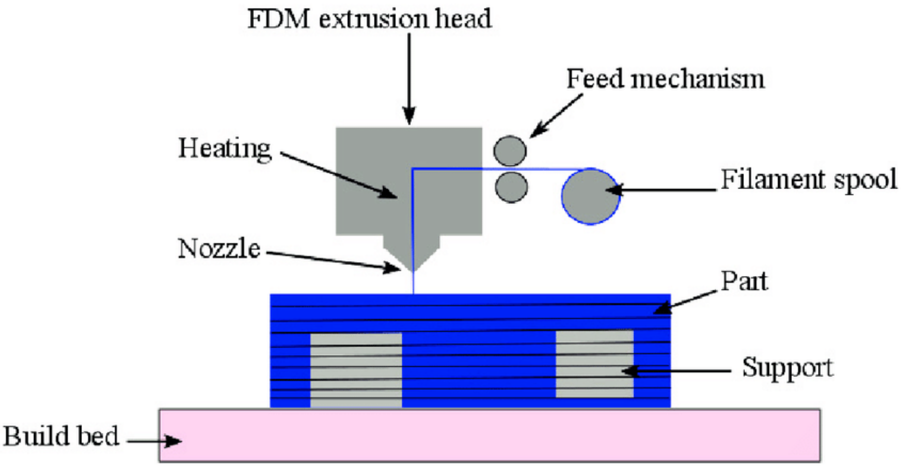

Figure 1.4: FDM Process[7]

1.2.2 AM for Space industry

AM processes apply incredibly well to the space industry where part production is low volume, highly customized and always aiming for mass reduction. Let's see some example of additive manufacturing being used in this sector:

- Companies like NASA and SpaceX already utilize additive manufacturing technologies to produce spacecraft components like brackets, mounts or entire structural elements.

- The production of components for rocket engine, like a turbopump with less parts and significantly lighter than the traditional manufactured counterpart.

- In satellites AM produced parts are already present , for example antennas support brackets or deployable structures.

- In-space manufacturing: thanks to 3D printing, on the ISS some tools and parts have been manufactured. This technology could open so many doors for future projects and even for Habitat construction in future missions.

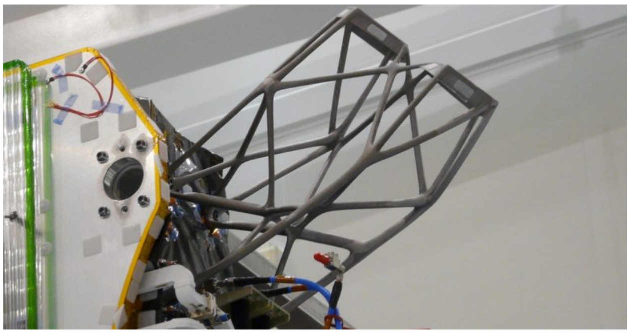

Figure 1.5: Antennas support for Koreasat-7 by Poly-shape in collaboration with Thales Alenia Space.[8]

1.3 Previous work

During the past decade or so, some efforts have been made in trying to utilize AM processes for the creation of CubeSats structure.
CRP Technologies was the first company to develop parts for the RAMPART satellite, a 2U CubeSat, using selective laser sintering technology to build the structure of the satellite. They utilized a proprietary polyimide based carbon material, the Windform XT, which has shown very low level of outgassing during space qualification. The RAMPART CubeSat mission has been successful and the material is now being used in other CubeSat projects.[5]

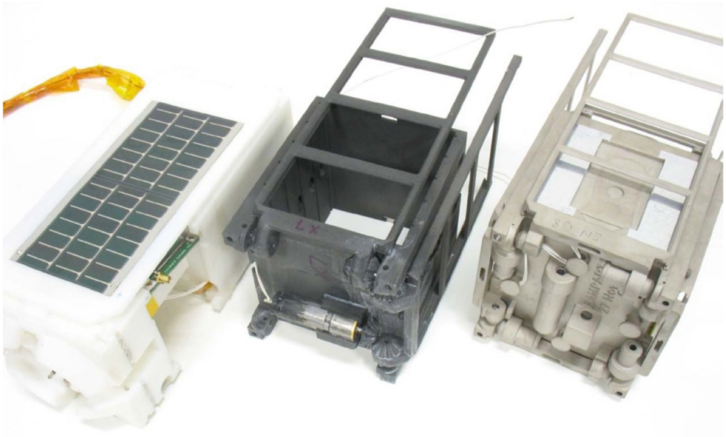

Figure 1.6: RAMPART CubeSat design stages [9]

In 2013 a student from the San Josè State University wrote his thesis on design and development of a CubeSat using AM processes. In his case it was a 1U CubeSat structure that was designed but also an attempt of payload design was made. This was done to recreate something as close to reality as possible. Everything was printed in ABS material which was also characterized and tested for outgassing in the limits of a University environment. The structure was also tested using FEM analysis and passed all the testing requirements but no experimental testing was done on the structure. In the figure below it is shown the completely printed CubeSat.[10]

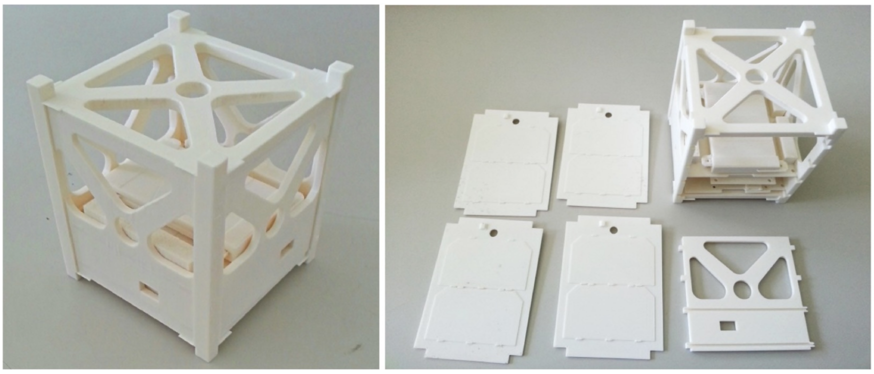

Figure 1.7: ABS Printed CubeSat [10]

In 2021 the article "Additive manufacturing of polyether Ether Ketone (PEEK) for

Space Applications: a Nanosat Polymeric Structure" was published by the University of Rome "Tor Vergata" in collaboration with Thales Alenia Space Italia and ESA. In the article an optimized structure for a 1U CubeSat is designed using a topological optimization. A mechanical characterization was done on the PEEK material using tensile and flexural test. An outgassing test was also done on the material and the requirements were fully satisfied. The design was then printed using an FDM process. The structure in this case didn't really satisfy all the design requirements but it wasn't the real focus of the paper.

Figure 1.8: PEEK Printed CubeSat [11]

1.4 Space & launch environment

During the Launch and ascent phases of the flight a lot of harsh environments are created due to vibration and acoustic. They affect all the launch vehicle and its payloads (CubeSats) which can include critical parts like solar panels and antennas.
These loads are a consequence of the interaction between the rocket engine exhaust mixing with the atmosphere or those mixing bouncing on the launch pad and into the exhaust again.
In addition, there are vibration generated due to engine shutdowns, wind gusts and quasi static loads. These loads can cause vibration environments of Acoustic, Random, Sine and shock origin. In the table below each of these origin is associated with a phase of the ascent phase.

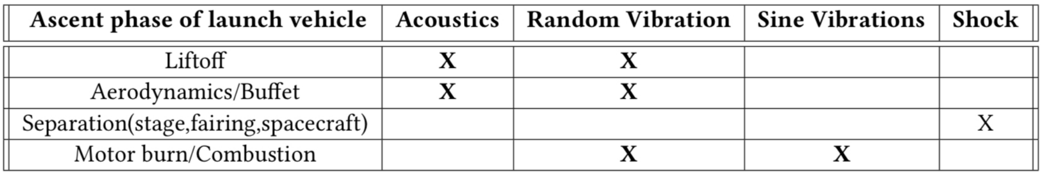

Ascent phase of launch vehicle	Acoustics	Random Vibration	Sine Vibrations	Shock
Liftoff	X	X		
Aerodynamics/Buffet	X	X		
Separation(stage,fairing,spacecraft)				X
Motor burn/Combustion		X	X	

Figure 1.9: Souces of launch vehicle environments [12]

The primary, secondary, and other components of a spacecraft or space system are designed and sized based on the maximum loads experienced throughout its life cycle, known as flight limit loads. These dynamic mechanical loads include:

- Handling loads

- Transportation loads
- Vibration test required for qualification of the spacecraft structure
    - Sinusoidal vibrations
    - Random vibrations
    - Acoustic pressure
- Dynamic loads during launch
    - Steady-state acceleration (inertia loads)
    - Sinusoidal vibrations
    - Random vibrations
    - Acoustic loads
    - Shock loads
    - Pressure variations
- In-orbit loads
    - Extension of folded elements, such as solar panesl, antennas, etc
    - Temperature gradients
    - 0 g loads
    - Micro-meteorite/debries impact

1.4.1 Environmental testing

To be sure that the satellite will be able to withstand this type of conditions, it must pass all the environmental testing procedures. Here are some common examples:

1. Thermal Vacuum Testing: this test simulates the vacuum and temperature extremes of space. The test verifies the performance of thermal control systems, materials, and components under realistic space conditions.
2. Vibration Testing: vibration tests simulate the mechanical stresses experienced during launch and ascent. This test ensures that the satellite's structural integrity and electronic components can withstand the mechanical loads without damage or malfunction.
3. Shock Testing: shock tests assess the satellite's ability to withstand sudden impacts and jolts, such as those caused by stage separations or deployment mechanisms.
4. Electromagnetic Compatibility (EMC) Testing: EMC testing evaluates the satellite's susceptibility to electromagnetic interference (EMI) and its ability to operate without causing interference to other systems.
5. Radiation Testing: radiation tests assess the satellite's resilience to the ionizing radiation present in space, including solar radiation, cosmic rays, and charged particles trapped in Earth's magnetosphere.
6. Humidity Testing: humidity tests evaluate the satellite's resistance to moisture ingress and humidity fluctuations.

The most important one for this thesis is going to be the vibration testing.

Chapter 2

Theory of Mechanical Vibration

2.1 Mechanical Vibration

Most human activities involves vibration in one form or another. For example, breathing is associated with the vibration of lungs and walking involves periodic oscillatory motion of legs and hands.

Any motion that repeat itself after an interval of time is called as Vibration Oscillation [13].

In essence, a vibratory system comprises components for storing potential energy (like a spring or elasticity), for storing kinetic energy (such as mass or inertia), and for dissipating energy (like a damper). The oscillation of such a system entails the conversion of potential energy into kinetic energy and vice versa, cyclically. When damping is present, energy dissipates during each vibration cycle, necessitating external assist to sustain a steady vibration state.

Vibrations in general is present in all mechanical systems, they could be beneficial or could lead to catastrophic situation. Some beneficial example are:

- Medical Imaging: Technologies like ultrasound utilize mechanical vibrations to produce images of internal body structures for diagnostic purposes, providing non-invasive insights into medical conditions.

- Musical instruments: Mechanical vibrations play a fundamental role in musical instruments, contributing to their sound production.

But on the other hand in some cases can be the exact opposite:

- Failure in turbine due to excessive vibration of the blades or disks.

- Excessive vibration of the satellite during launch could cause the destruction of the satellite itself and of the launcher.

- Earth quakes are vibration of the earth soil that can cause the structures of the buildings to fail.

2.2 Important definitions

The **Natural Frequency** of a system is the frequency at which it would vibrate if it was allowed to move freely and no external force was applied on it. It is also known as the characteristics frequency, resonant frequency, normal frequency or fundamental frequency.
At its natural frequencies the patterns of vibration exhibited by the system represent its **Mode shapes**. When a system is excited, such as by an external force or impulse, it vibrates in a specific manner determined by its geometry, material properties, and boundary conditions. The mode shapes describe how different parts of the system move relative to each other during vibration.
When the natural frequency of the system coincides with the frequency at which the external force/load applied is oscillating, then **Resonance** occurs. At resonance the accelerations of the system increase, the system vibrate violently and with higher amplitudes.
Sometime resonance can bring the system to a total collapse like in the Takoma Narrows Bridge case in 1940. Strong winds caused the bridge to vibrate at its natural frequency, resulting in a phenomenon known as aeroelastic flutter. The bridge oscillated violently until it collapsed into the Tacoma Narrows strait, just a few months after its completion.

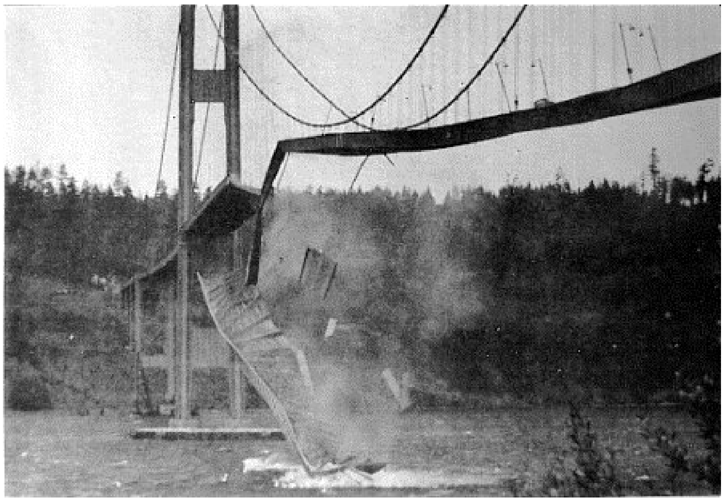

Figure 2.1: Tacoma Narrows bridge collapse in 1940 [13]

2.3 Degrees of freedom

"The minimum number of independent coordinates required to determine completely the positions of all parts of a system at any instant of time defines the number of degrees of freedom of the system" .[13]
In the real world, structures are set to have an infinite number of degree of freedom but when we analyze them we simplify them and bring this number to a finite number. In figure 2.2 and 2.3 some examples are shown:

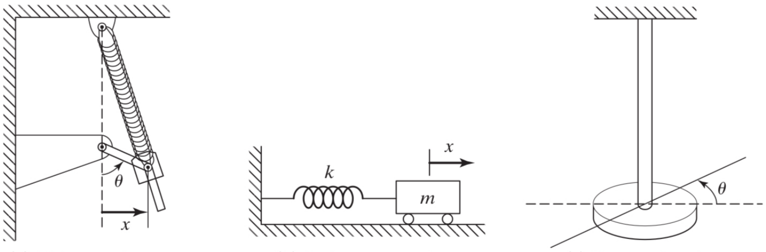

(a) Slider-crank-
spring mechanism

(b) Spring-mass system

(c) Torsional system

Figure 2.2: One-degree-of-freedom systems [13]

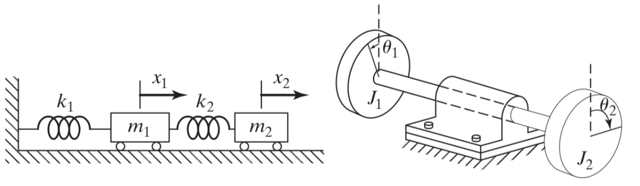

(a)

(b)

Figure 2.3: Two-degree-of-freedom systems [13]

2.4 Classification of Vibration

Vibration can be classified in a lot of different ways. Here are some of the most important:

Free and Forced vibration

- Free Vibration: no external force acts on the system that is left to vibrate on its own after an initial disturbance.
- Forced Vibration: the system is subjected to an external force, the resulting vibration is known as forced vibration. If the frequency of the external force is the same as the natural frequency of the system than the resonance phenomenon occurs.

Undamped and damped Vibration "If no energy is lost or dissipated in friction or other resistance during oscillation, the vibration is known as undamped vibration."[13] On the contrary if some energy is lost then it is called damped vibration.

Deterministic and Random Vibration If at any moment in time the value or the magnitude of the excitation force is known then the resulting vibration of the vibratory system is called deterministic.
When the values of the excitation is random it can't be predicted. It is possible in some cases estimate averages such as mean and mean square value of the excitation. The resulting vibration is called Random. The vibratory response of the system will also be random[13].

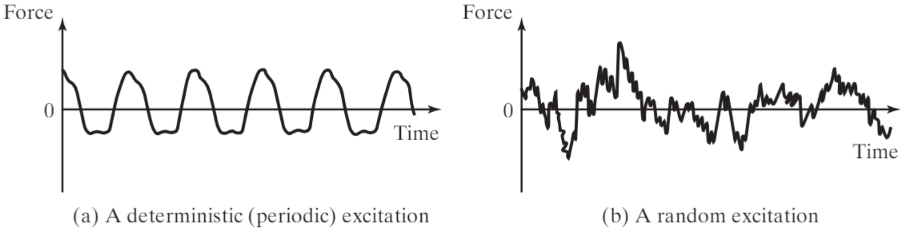

(a) A deterministic (periodic) excitation

(b) A random excitation

Figure 2.4: Deterministic and random excitation [13]

2.5 Equations of motion

The simplest method to analyse a dynamic system is using the equation of motion method. We can start from a single degree of freedom (SDOF) model to introduce it and then expand it to a multi degree of freedom (MDOF). The model is composed by a mass, a spring and a dumper. The model is shown in figure 2.5.

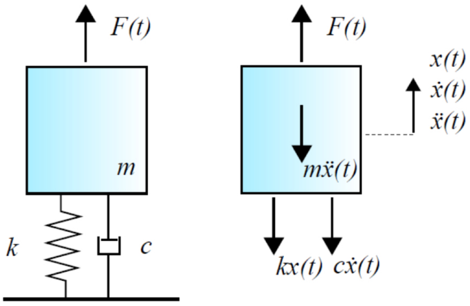

Figure 2.5: SDOF system [14]

Some assumption are made: the spring and the dumper are massless, the mass **m** moves only in the vertical direction and a time dependent force **F(t)** is applied vertically on the mass **m**. F(t) can be of any type: constant, harmonic, rectangular or random. Now it is possible to analyse the free body diagram, the result is the equation below.

$$m\ddot{x}(t) + c\dot{x}(t) + kx(t) = F(t) \tag{2.1}$$

This is the equation of motion for a single degree of freedom system.
When a multi degree of freedom needs to be analyse the equation remains the same in its form but the mass, the dumper coefficient and the spring stiffness become matrices.

$$\mathbf{M}\ddot{x}(t) + \mathbf{C}\dot{x}(t) + \mathbf{K}x(t) = \mathbf{F(t)} \tag{2.2}$$

2.5.1 Vibration response of an undamped system

Taking into consideration the one degree freedom system in the figure 2.5 and the equation of motion 2.1 we can make a simplification, given the problem is undamped the value of $\mathbf{c} = 0$. Now the equation of motion is:

$$m\ddot{x}(t) + kx(t) = F(t) \tag{2.3}$$

The solution of this equation is the some of two different solution: the homogeneous and the particular. The homogeneous solution is the solution of the same problem when the F(t) is set to 0:

$$m\ddot{x}(t) + kx(t) = 0 \tag{2.4}$$

The harmonic solution is assumed:

$$x_h = Asin(\omega t) + Bcos(\omega t) \tag{2.5}$$

A and B are only dependent on the initial conditions x(0) and $\dot{x}(0)$.
Now if the 2.5 is punt in the 2.4 we find the following:

$$A(k - m\omega^2)sin(\omega t) + B(k - m\omega^2)cos(\omega t) = 0 \tag{2.6}$$

The solutions to this equation is A = B = 0 or:

$$\omega_n = \sqrt{\frac{k}{m}} \tag{2.7}$$

which represent the natural frequency of the system.
The other part of the solution to the 2.1 equation is the particular solution (x_p) that depend only on the external force that is applied and its type[14].

2.5.2 Effect of the damping

Like it is said at the beginning of this chapter the damping is the mean through which the system dissipate the energy. If the dumping is present, then the homogeneous equation of motion can be rewritten as:

$$\ddot{x}(t) + 2\zeta\omega_n\dot{x}(t) + \omega_n^2 x(t) \tag{2.8}$$

where $\omega_n = \sqrt{k/m}$, $\zeta_n = \sqrt{c/(2m\omega_n}$. ω_n is the natural frequency for the undamped system and ζ is the damping ratio. The system can be characterised based on this damping ratio:

- Undamped system: $\zeta = 0$;
- Underdamped system: $\zeta < 1$;
- Critically system: $\zeta = 1$;
- Overdamped system: $\zeta > 1$;

The homogeneous solution to the damped system is:

$$x_h = e^{-\beta t}(Asin(\omega_d t) + Bcos(\omega_d t)) \tag{2.9}$$

where $\beta = \frac{c}{2m} = \zeta\omega_n$ and $\omega_d = \omega_n\sqrt{1 - \zeta^2}$ is the dumped frequency.

2.5.3 Response to the excitation of the base

When the excitation force comes from another mass connected the first one the system evolve and the figure 2.6 shown the new model:

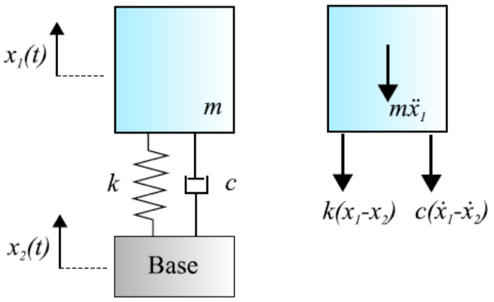

Figure 2.6: SDOF system with excitation base [14]

The equation in this case is:

$$m\ddot{x}(t) + c\dot{x}(t) + kx(t) = -m\ddot{x}_2(t) \tag{2.10}$$

The x_2 is known and the x_1 is unknown. The problem can be solved the same way as before.
Another concept that can be undertood better from this example is the resonance. Let's introduce a new parameter, the Transmissibility ratio TR:

$$TR = \frac{\ddot{x}_{1,max}}{\ddot{x}_{2,max}} \tag{2.11}$$

where $\ddot{x}_{1,max}$ and $\ddot{x}_{2,max}$ are the maximum values of acceleration of the base and of the mass. Now it important to see the trend between TR and the ratio between the frequency at which is vibrating the system and the natural frequency of the system.

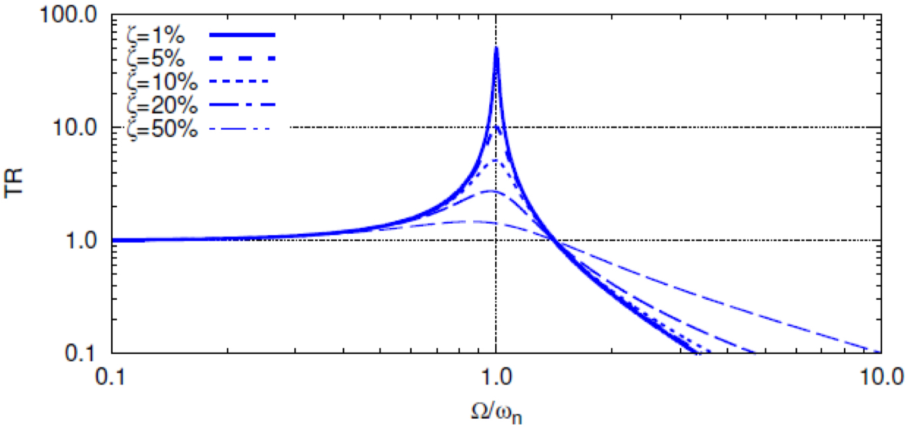

Figure 2.7: Transmissibility ratio [14]

Looking at the figure 2.7 an observation can be made: when the value of the frequency ratio come close to the value of 1 the TR increase by a lot which means that when the

excitation frequency Ω (frequency of the base) is close to ω_n, the response of the mass in terms of acceleration increase vertiginously creating the resonance effect. This effect is mitigated by the damping factor, the higher it is the less amplified is the response of the mass.
There are two important zones that can be seen in the figure:

- $0.6 < \Omega/\omega_n < \sqrt{2}$ is the amplified zone. When the structure is designed it is important to avoid staying in this zone.
- $\Omega/\omega_n > \sqrt{2}$ is the mitigated zone. In this zone the response of the mass in terms of acceleration is less than then the one that the base is creating.

2.6 Frequency domain analysis

The frequency domain analysis of the system is useful it gives a lot more information about the system itself compared to the time domain counterpart.
The main step consist in express the time dependent force F(t) in Fourier series. From this point it is possible to find the response of system x(f) by multiplying the force F(t) for a Transfer Function H(f).

$$H(f) * F(t) = \text{Output}$$

H(f) is complex valued function so it is composed by a real and an imaginary part.
We can also find the amplitude and phase of the function using the following formulas:

$$|H(f)| = \sqrt{Re(H)^2 + Im(H)^2}$$

$$\phi(f) = tan^{-1}(\frac{Im(H)}{Re(H)})$$

All the parts of the transfer function can be plotted and from there extrapolate important information. The real part of the FRF will equal zero at natural/resonant frequencies. The imaginary will have "peaks" either above or below zero which indicate resonant frequencies. If several FRFs are acquired at different locations on the structure, and they are all phased with respect to a common reference, the imaginary part of the FRFs can be used to plot the mode shape.

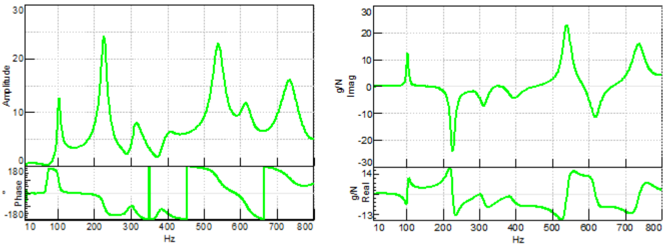

Figure 2.8: FRF examples [15]

Chapter 3

Theory of Vibration Testing

3.1 Instrumentation

Conventional experimental modal analysis techniques involve applying a vibrational force to the structure using either an impact hammer or a shaker system. Force transducers measure the input force, while motion transducers capture the resulting vibration response. These signals are then digitized and processed by an analysis system to estimate the frequency response functions (FRFs) of the structure. Once the FRFs are obtained, the analysis system can determine the modal characteristics, such as natural frequencies, mode shapes, and damping ratios, that describe the dynamic behavior of the structure.[16]

3.1.1 Force Transducers

In conventional modal analysis set-ups, piezoelectric force transducers are widely employed. These transducers leverage the piezoelectric effect, where the application of a force on the crystal structure generates a proportional electrical charge. The key performance characteristics of these force transducers include their maximum force capacity, frequency response limits, and sensitivity, which directly impact the quality and reliability of the measured force data.[16]

3.1.2 Motion transducers

Motion transducers are employed to measure the system's dynamic response, with accelerometers being the most commonly used option due to their relatively low mass compared to displacement or velocity transducers. One key advantage of accelerometers is that their acceleration signals can be readily integrated electronically to obtain velocity and displacement data.

An accelerometer operates as a mass-spring-damper system, generating an output signal proportional to the acceleration within a frequency range well below its natural resonance. A critical aspect in using accelerometers is the method of attachment to the structure. Threaded stud mounting provides the most robust connection but requires pre-drilled threaded holes. Alternative attachment techniques include the use of beeswax or, for ferromagnetic surfaces, a permanent magnet. Various other mounting options are also available.

Equally important is the precise placement of the accelerometer, as it must be positioned at the exact location where the desired vibration measurement is to be taken to ensure the data accurately represents the local dynamic behavior.[16]

3.1.3 Hammer testing

Hammer testing, also known as impact testing or modal impact testing, is a widely used method in experimental modal analysis to excite a structure and measure its dynamic response. The primary advantage of hammer testing is that it does not require any equipment to be attached to the structure, so the excitation system does not influence the dynamics of the test object. This makes the set-up simpler and quicker, ideal for field applications or when testing time is limited.

In hammer testing, a structure is struck with an instrumented hammer that has a built-in force transducer to measure the input force. The aim is to generate a specific force level over a defined frequency range. The impact of the hammer produces a relatively smooth force spectrum up to a certain frequency. The energy level and frequency span of the impact are determined by several factors, including the force applied by the user, the hammer's weight, the hardness of the hammer tip, and the compliance of the impact point on the structure. For instance, to reach higher frequencies, a shorter impact duration is required, which can be achieved using a harder tip—this is particularly effective for lightweight and relatively stiff objects.

The correct choice of hammer tip is crucial, as it should generate enough energy to excite the full frequency range of interest without significantly exceeding it. Additionally, the tip ensures that sufficient force is applied to excite the relevant modes of the structure. However, hammer testing also has some disadvantages. The concentration of energy in a very short time can cause overloading, leading to potential measurement errors. Furthermore, multiple strikes may be necessary when testing larger structures to ensure that the entire system's response is adequately captured. Despite these challenges, hammer testing remains a valuable tool for quickly diagnosing the dynamic characteristics of structures, especially when a non-invasive or portable testing solution is required.

Figure 3.1: Hammer testing set-up[17]

3.1.4 Shaker testing

Shaker testing is another widely used method in experimental modal analysis for exciting structures and measuring their dynamic response. Unlike hammer testing, shaker testing involves a more controlled and continuous excitation of the structure, which allows for a more precise and detailed analysis of the system's behavior across a wide frequency range.

Since the excitation is applied gradually and continuously, it is easier to avoid damaging the structure or distorting the measurements due to excessive force. Additionally, shaker testing is ideal for testing larger structures or those with complex geometries, where a more uniform excitation is required to capture the full dynamic behavior.

In shaker testing, the shaker is connected to the structure through a stinger or load rod. This connection is crucial as it influences the accuracy of the measurements. Ideally, the connection should be stiff in the direction of measurement to ensure accurate force transmission, while being flexible in other directions to minimize interference with the structure's natural dynamics. Despite these precautions, the attachment of the shaker can still slightly affect the measurement by introducing additional mass or stiffness, so it's important to minimize these effects as much as possible.

The testing set-up also includes additional equipment, such as a signal generator that produces the excitation signal. This signal can take various forms, such as sine sweeps, random noise, or broadband excitation, depending on the specific analysis needs. The variety of excitation signals available in shaker testing is one of its key advantages, allowing for a thorough investigation of the structure's dynamic behavior across different conditions.

However, shaker testing does come with its challenges. The set-up is significantly more complex and time-consuming compared to hammer testing. Proper alignment and secure attachment of the shaker and associated equipment are essential for accurate results, and this can be difficult to achieve, especially in field environments. The equipment used in shaker testing is also bulkier and less portable, making it less convenient for quick tests.

Despite these challenges, the benefits of shaker testing, including its ability to provide precise, controlled excitation and the wide range of excitation signals available, make it an invaluable tool for in-depth modal analysis, particularly in laboratory settings where high accuracy is required.

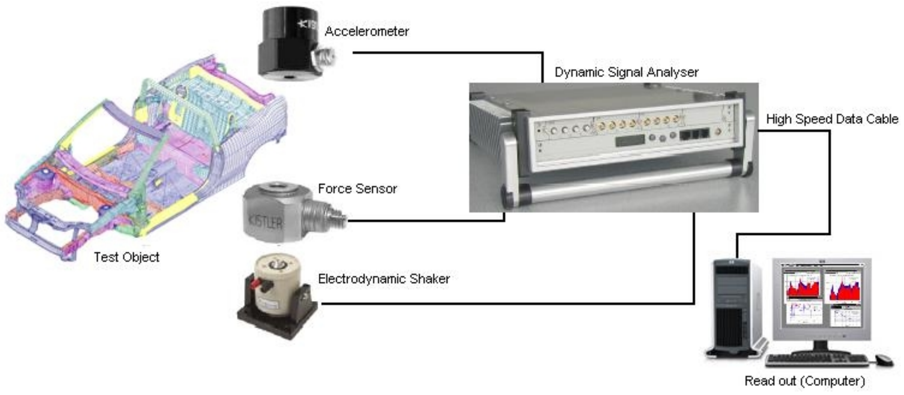

Figure 3.2: Shaker testing set-up[17]

3.2 Test Set-up

The complexity of the test set-up depends heavily on the specific objectives and requirements of the modal analysis. A key principle in designing an effective experimental set-up is to leverage all relevant information available, such as results from previous tests on similar structures or pre-test finite element analyses.[16] libro ku leuven (guarda foto)

3.2.1 Suspension and boundary conditions

The connection between the test object and its surrounding environment is a critical consideration, as the suspension method employed depends directly on the specific objectives of the modal analysis. When seeking to correlate test results with a finite element model (FEM), it is crucial to ensure the test boundary conditions closely match those assumed in the analytical model.
For example, to simulate free-free conditions similar to the in-space environment, the test article can be suspended using soft springs. This suspension approach minimizes the influence of external constraints on the structure's dynamic behavior. In contrast, satellites experience two primary boundary conditions during their lifecycle - a free-free state in the space environment, as well as a fixed-base condition when integrated within the launch vehicle. Accurately replicating these distinct boundary conditions during testing is essential for validating the analytical models and ensuring the test data is representative of the real-world scenarios.[16]

3.2.2 Excitation

As mentioned in the previous section, the two primary methods of vibration excitation are the impact hammer and the shaker system.
To better capture the structure's resonant behavior during these modal tests, the use of multiple input excitation is becoming increasingly common. Multi-input measurements can provide more consistent and comprehensive data, albeit requiring a slightly longer test duration. This approach involves applying vibration inputs to the structure using two or more shakers positioned at different locations and oriented in diverse directions. By distributing the excitation across multiple points on the structure, the multi-input technique is able to more effectively stimulate the various vibration modes of interest. This is particularly advantageous compared to single-input tests, where certain modes may not be adequately excited due to the limited force application location and direction. Incorporating this multi-input, multi-directional excitation strategy into the test set-up enables a more thorough and reliable characterization of the structure's modal properties, ultimately enhancing the correlation with analytical models and the overall design validation process.[16]

3.2.3 Response locations

The number of response locations depends on factors such as the frequency range of interest, the number of expected modes, the areas of the object under investigation, the number of available transducers, and the time available for testing. Higher frequency modes require more response locations to accurately capture the modal behavior. If the goal require to validate a finite element model (FEM), it is beneficial to have as many measurement locations as there are degrees of freedom in the model.[16]

3.3 MIMO random control theory

MIMO (Multiple Input, Multiple Output) testing is a sophisticated technique used in vibration testing to simultaneously excite and measure multiple points on a structure. This method provides a comprehensive view of the dynamic behavior of complex systems by allowing for the simultaneous application of multiple excitation sources and the collection of response data from various locations.[18]
By using multiple inputs and outputs, MIMO testing can provide more accurate and detailed data on how different parts of a structure interact with each other. This is particularly useful for complex structures where single-input testing might not capture the full dynamic response.
The general advantages of MIMO testing are: it's detailed understanding of the structure's dynamic behavior achieved by capturing interactions between multiple excitation sources and response points and it's efficiency in terms of testing time in respect to sequential type of testing like a SIMO test. This advantages comes with a price in terms of complexity of the set-ups and a more challenging data interpretation because of the interaction between the multiple inputs and outputs.
In the context of vibration control testing, there are several types of Multi-Axial Vibration Control qualification tests that differ, one from the other, from the nature of the excitation environment that needs to be applied on the specimen:

- MIMO Random Test
- MIMO TimeWaveform Replication
- MIMO Sine Control Test

The one that is going to be used in this thesis is the MIMO Random test.

The Random vibration control test in general is very much utilized in the testing of components in every major mechanical system from automotive to aerospace. In particular is one of the qualification tests that a satellite of any dimension has to pass in order to be on the launch vehicle. It consist in applying a random signal that has an average acceleration defined by a profile, usually in terms of PSD (Power Spectral Density) that needs to be reproduced in certain control channel location, over a specified frequency range, this way all frequency components in the testing range are present at the same time. The advantage of this type of test is the fact that all the frequencies are excited simultaneously so also the resonances are excited at the same time which can bring to a different result than exciting the various resonances at different times. In the SIMO Random control test, the direction of the excitation is only one, as it is the qualification requirement profile needed. This brings some limitation in terms of how similar the test is to reality where the excitations typically come from different directions at the same time. This limit can be overcome using MIMO Random Control. The qualification requirement, in this case, are given in terms of PSDs but that isn't sufficient, additional information about how the control channel needs to interact between each other are needed. This information needs to be provided in terms of CSDs (Cross Power Spectral Density) between the control channels. This is done by, for example, defining the desired phase and coherence. The target of a MIMO random control test is thus a full reference Spectral Density Matrix (SDM).
This is not as straight forward as it seems, because a-priori the cross-correlation between

channel is not known and just filling the off-diagonal terms doesn't guarantee that the reference matrix has a physical meaning.
The best information an environmental engineer can use as target is a real life recording or field data, but even in this case it is possible that some differences between the field and laboratory conditions could create problems in the control.

3.3.1 Algebraic theory

A general MIMO linear system can be represented by m inputs and l outputs that are linked by what in this case is the the structure under testing represented by the Frequency Response Function (FRF) matrix (figure 3.3. The input and outputs can be represented by two vectors **u**(t) and **y**(t) of dimension m x 1 and n x 1 respectively.

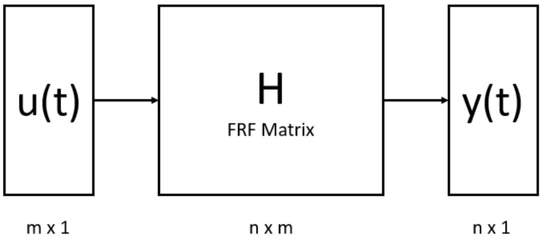

Figure 3.3: MIMO linear system

Both input and output are vectors in the time domain but can be represented also in the frequency domain, **U**(f) and **Y**(f), using the Fourier Transform remembering that now U and Y are complex numbers.
The system can be written as

$$\mathbf{Y} = \mathbf{HU} \tag{3.1}$$

Multiplying by U' both side of the equation, it can be rewritten as

$$\mathbf{YU'} = \mathbf{HUU'} \tag{3.2}$$

Now new component can be defined thanks to this operation[19]:

- $\mathbf{S}_{uu} = E[\mathbf{UU'}]$ is the Input spectral Density Matrix with a dimension of m x m
- $\mathbf{S}_{yy} = E[\mathbf{YY'}]$ is the Output spectral Density Matrix with a dimension of n x n
- $\mathbf{S}_{yu} = E[\mathbf{yU'}]$ is the Cross spectral Density Matrix with a dimension of n x m

Substituting the definition of the Spectral Density Matrices in the equation 3.2

$$\mathbf{S}_{yu} = \mathbf{H}\ \mathbf{S}_{uu} \tag{3.3}$$

The initial estimation of the frequency response function (H) can be computed based on a set of uncorrelated random input signals. This system identification process involves leveraging the input and cross-spectral density matrices, which can be estimated using techniques such as Welch's Averaged Periodogram method.

$$\hat{H} = \hat{S}_{yu}\hat{S}_{uu}^{\dagger} \tag{3.4}$$

From the linear MIMO system, a control system is needed for Random Control. The objective of a control system is to create a drive signal vector, u(t), which causes the Output Spectral Density Matrix, S_{yy}, to agree within some acceptable margin, with the user specified Reference Spectral Density Matrix, S_{yy}^{ref}.

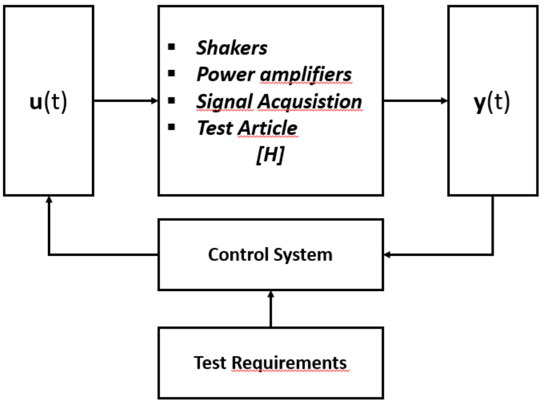

Figure 3.4: MIMO linear system[18]

In theory it is always possible to determine the Input SDM (S_{uu}) starting from the user defined Reference SDM (S_{yy}) with the inverse control problem [18]

$$\begin{aligned} Y &= HU \longrightarrow U = H^{\dagger}Y \\ U' &= (H^{\dagger}Y)' = Y'H^{\dagger\prime} \\ UU' &= H^{\dagger}YY'H^{\dagger\prime} \\ S_{uu} &= H^{\dagger}S_{yy}^{ref}H^{\dagger\prime} \end{aligned} \tag{3.5}$$

The eq. 3.5 shows how, to define the Output-to-Input relationship, the inverse of the FRF matrix H is needed. This matrix inversion needs to be performed carefully as singularities can exit at various frequencies.
It's easy to see that the system identification has a critical role in the success of a MIMO control test.

3.3.2 Reference Spectral Density Matrix

In MIMO Random Control not only the vibrations at each specified control location need to be verified, but also the vibration relations that exist between each set of control points. In this sense, the target that needs to be reached during the test must be a full Spectral Density Matrix where the cross terms are as important as the diagonal ones. Therefore the challenges of MIMO Random Control start even before the actual test, in the test definition stage. Just filling the reference matrix does not guarantee a physical meaning. In order to be sure of the fact that the SDM is realizable it needs to be a semi-definite positive matrix. This means that one of this requirements have to be met[21][22]:

1. all eigenvalues of S_{yy}^{ref} are semi-positive;
2. S_{yy}^{ref} has a unique Cholesky Decomposition, meaning that it can be decomposed in the product of two triangular hermitian matrices, referred as the Cholesky Factors: $S_{yy}^{ref} = LL'$.

Moreover, if S_{yy}^{ref} is semi-positive then:

- the trace of S_{yy}^{ref} is real and semi-positive, being the matrix trace the sum of its eigenvalues;
- the determinant of S_{yy}^{ref} is real and semi-positive, being the matrix determinant the product of its eigenvalues
- $S_{uu} = ZS_{yy}^{ref}Z'$ is semi-definite.

As already said before the Reference Spectral Density is a combination of PSDs and CSDs and for a generic system with l control points is shown in figure 3.5.

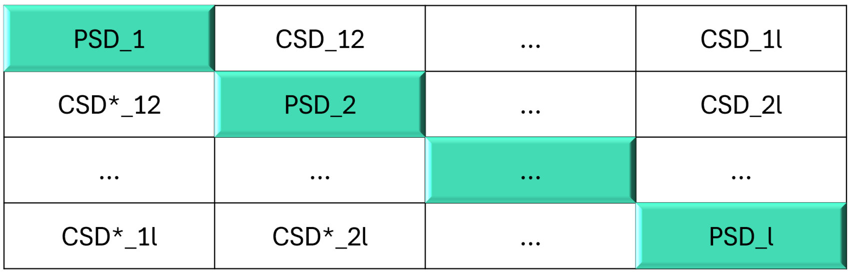

PSD_1	CSD_12	...	CSD_1l
CSD*_12	PSD_2	...	CSD_2l
...	...	...	...
CSD*_1l	CSD*_2l	...	PSD_l

Figure 3.5: Reference Spectral Density Matrix of l control

The cross-terms are often unknown quantities and need to be defined. They can be determined from the respective PSDs using the following equation:

$$CSD_{ij} = |CSD_{ij}|e^{i\phi_{ij}} = \gamma_{ij}\sqrt{PSD_iPSD_j}e^{i\phi_{ij}} \tag{3.6}$$

where the i and j correspond to the i-th and j-th control channels, γ_{ij} and ϕ_{ij} are respectively the coherence value and the phase angle between the two control channels. In the MIMO case , care must be taken in interpretation of coherence, because of its definition is closely related to eq.3.6. The coherence function is defined as the correlation coefficient describing the linear relationship between any two single spectra [18]

$$\gamma_{ij}^2 = \frac{|CSD_{ij}|^2}{PSD_iPSD_j} \longrightarrow 0 < \gamma_{ij}^2 < 1 \tag{3.7}$$

Considering two control channels on x and y direction, if the phase between them is zero ($\phi_{xy} = 0$), the movement will preferably occur along a 45° straight line . Moreover if the coherence is one, then movemen will occur on a straight line.
Using this definitions, lets take a look at an example. The software that is going to be used throughout this thesis is Simcenter Testlab by Siemens. The software has multiple functions and can be used for different tests. In particular for this case, the MIMO Random Control application is going to be used. The shaker is a 4-DOF shaker so the number of control channel needed is going to be four. The diagonal terms are defined by a PSD profile, like already talked about, and the off-diagonal terms are the coherence between the control channels. For computational reasons, coherence values of 0 and 1 are usually avoided and the typical values range from 0.05 and 0.98.

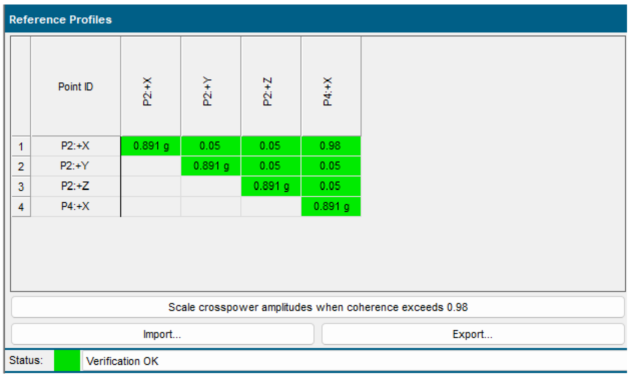

	Point ID	P2:+X	P2:+Y	P2:+Z	P4:+X
1	P2:+X	0.891 g	0.05	0.05	0.98
2	P2:+Y		0.891 g	0.05	0.05
3	P2:+Z			0.891 g	0.05
4	P4:+X				0.891 g

Status: 🟩 Verification OK

Figure 3.6: Example of Reference Spectral Density Matrix in Simcenter TestLab

Chapter 4

Design Process

4.1 CubeSats Design Regulations

The CubeSat Design Specification document was issued with the intent of reduce costs and developing time, increase accessibility to space, and sustain frequent launches. To create a CubeSat design we have to start from here.
Prior to a CubeSat being Manifested on a launch, the specifications and requirements stated in the CDS provide guidance on the CubeSat design. After that the Launch provider requirements supersede the CDS's.[1]
Let's start with the CubeSat's Mechanical Specification. The Rail constraint design will be the one used for all the design in this thesis. There is another type of constraint that can be used in the deployer, it uses a Tab instead of the rails, but it isn't utilized much at the moment. The dimensions of the CubeSat itself can be seen in the CDS drawings[1]. Here are now listed some of the other requirements or information that are not present in the drawings:

1. The -Z face of the CubeSat will be inserted first into the dispenser.
2. No components on the yellow shaded sides shall protrude farther then 6.5 mm normal to the surface from the plane of the rail.
3. Rails should have a surface roughness less than 1.6 μm
4. The edges of the rails should be rounded to a radius of at least 1 mm.
5. At least 75% of the rail should be in contact with the dispenser rails. 25% of the rails may be recessed[1]

The third requirement, if the structure is FDM produced, is highly unlikely to achieve but other measures can be taken into consideration.

4.2 Design for AM

If the structure is AM produced some other requirements and considerations will be provided by the process it self. In the FDM case are:

- Minimum Feature Size: FDM printers have limitations on the minimum feature size that can be accurately reproduced. Design features such as wall thickness, hole diameter, and text size should be larger than the printer's minimum resolution to ensure proper printing.

- Overhangs and Support Structures: FDM printing requires support structures for overhanging features and steep angles to prevent sagging or collapse during printing. Design overhangs at angles less than 45 degrees to minimize the need for supports.

- Fillets and Chamfers: Incorporate fillets and chamfers into the design to improve part strength, reduce stress concentrations, and enhance aesthetics.

- Tolerances and Shrinkage: Account for material shrinkage and dimensional tolerances when designing parts for FDM printing.

4.3 First Design

The idea behind the first design is to have the least amount of parts and connections possible to emphasise the characteristics of an AM produced product. Starting from the design constraint coming from the CDS a basic 1 part model have been design to first understand how it should look like and the envelope of the dimensions (figure 4.1).

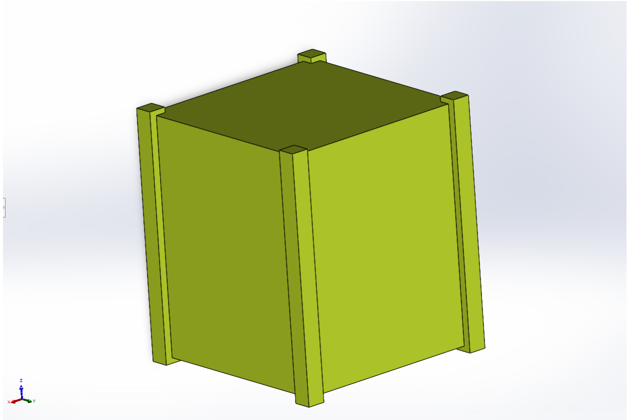

Figure 4.1: First iteration CubeSat

From there it was decided that a two part structure was achievable and in different ways too. The one used for this design consisted in dividing the cube in two parts, each with three faces and two rails.
The faces have a thickness of 4 mm to allow a good print, if they were too thin the structure could collapse during the printing process or leave spaces between layers.
All the faces were then lightened using self supporting design for the openings. The use of specifically designed openings will help in the manufacturing process (see chapter 5).
In the figure 4.2 the two separated parts of the CubeSat are shown.

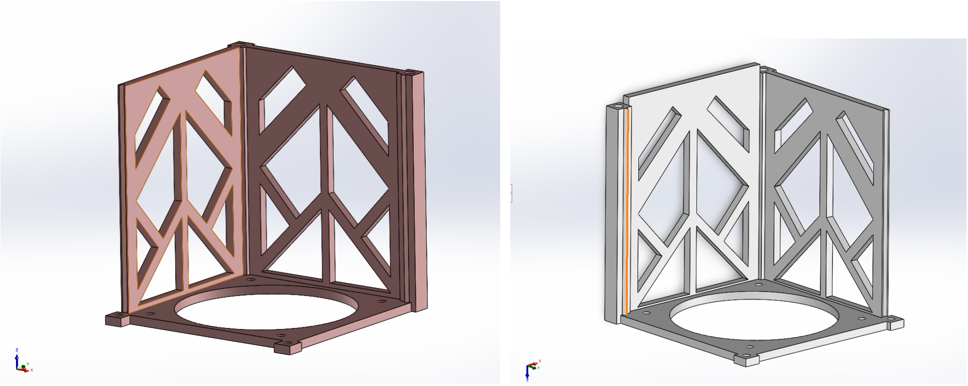

Figure 4.2: First design structure parts

The two parts are easily connected, another requirement that was important to obtain, by four screws, two in the top face and two at the bottom. Being this an AM produced part, for this connection to happen some inserts are also needed. In figure 4.3 it is possible to see the connections but without the threads used only as a reference in the CAD phase.

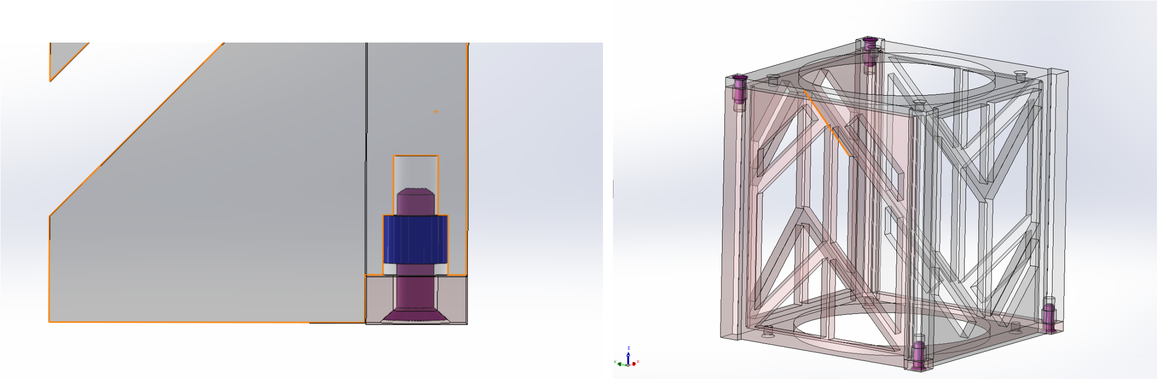

Figure 4.3: Connections between the 2 parts of the structure

If only the screws would have been used some parts of the structure could have been subjects of flapping during the vibration testing. To stop this phenomenon from happening, a triangular rail type of connection between the two part was established along two faces. The detail of the connection is shown in figure 4.4 but the extrusion or cut can also be seen from figure 4.2.

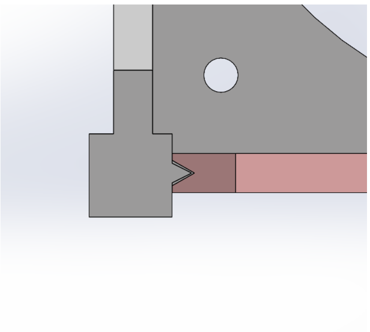

Figure 4.4: Triangular track like connection

A last image of the assembly is reported below.

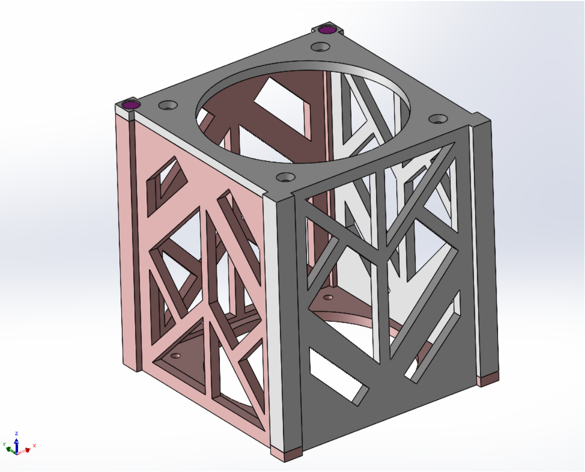

Figure 4.5: First design assembly

As it can be seen confronting figure 4.11 with the envelope in figure 4.1, some of the requirements are not met; in fact, the top and bottom faces were considered flat to completely eliminate the supports that would have been needed during the manufacturing process. Being the support difficult to remove from the PEEK printed parts those were eliminated using this design.
To have a more realistic design and comply with the CDS requirements two different very small parts were printed to create the ends of the rails. They can both be seen in figure 4.6.

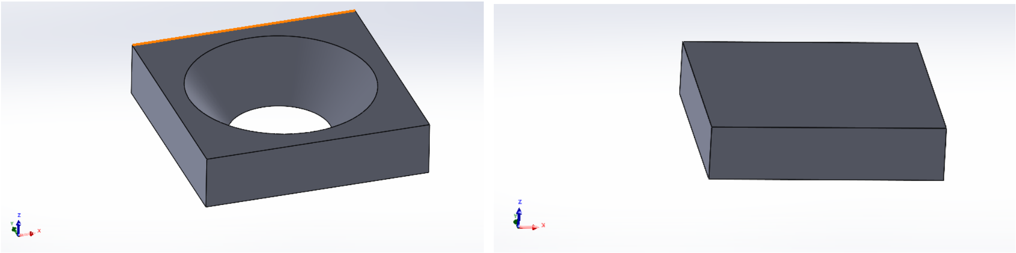

Figure 4.6: Added parts

The part with the hole is going to be used for the rails with the hole and are going to be connected through the same screw that was used before (figure 4.7 . The flat ones are going to be glued to the part itself in the right position.

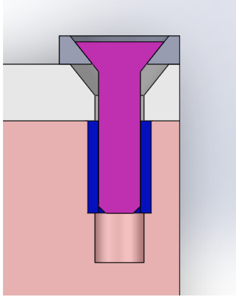

Figure 4.7: Total rail connection

Now looking at the complete assembly is possible to see that the design is correct and comply with the CDS.

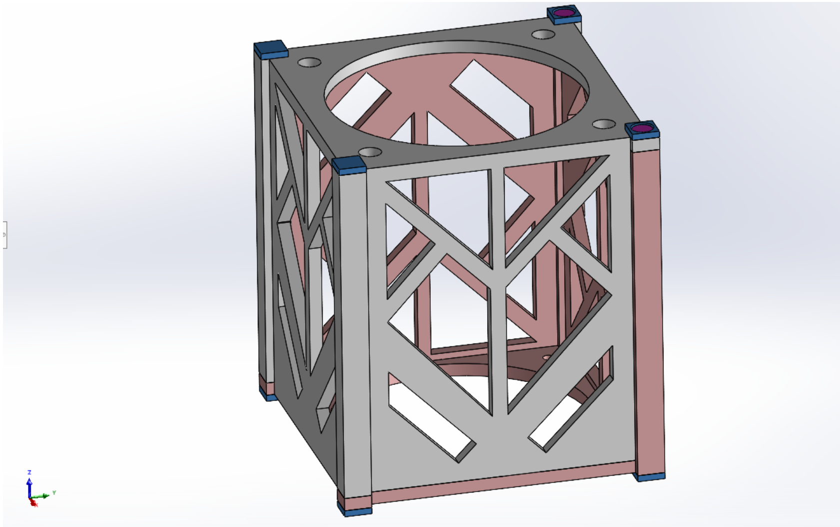

Figure 4.8: First design complete assembly

4.4 Second Design

For the second design the decision was to go in the complete opposite direction from the first. In fact, the design idea is taken from the structure that at the moment can be bought off the shelf, like the one in figure 1.5.
The structure itself is composed of two primary parts (figure **??**$1 \mod 1 Theplate :$
$therearegoingtobetwo, onefor the top and another one for the bottom with a thickness of 5mm. This thick$

The rails: four of them one for each angle

The parts are very simple themself too without any difficult feature to print.

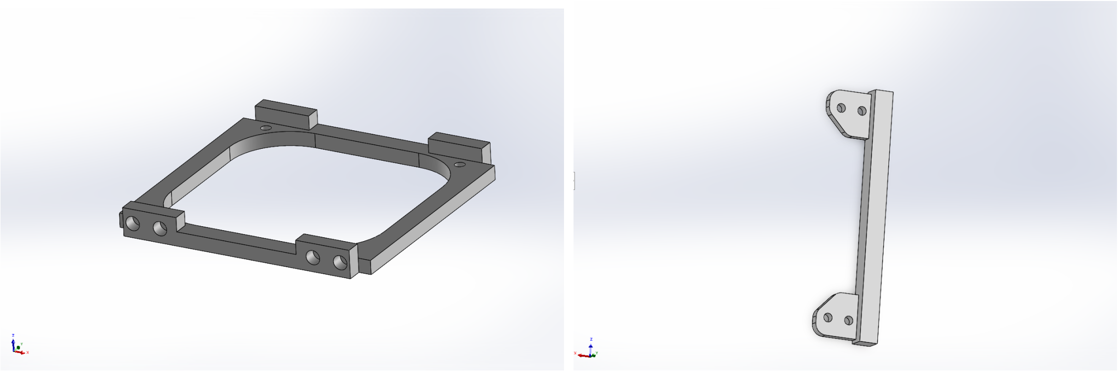

Figure 4.9: Plate and rail used

To connect these 6 parts, 16 screws with inserts are needed so that the structure is stiff enough (figure 4.10). This is one of the problems with the design that is currently used, it needs a lot more parts and connecting pieces than the first design.

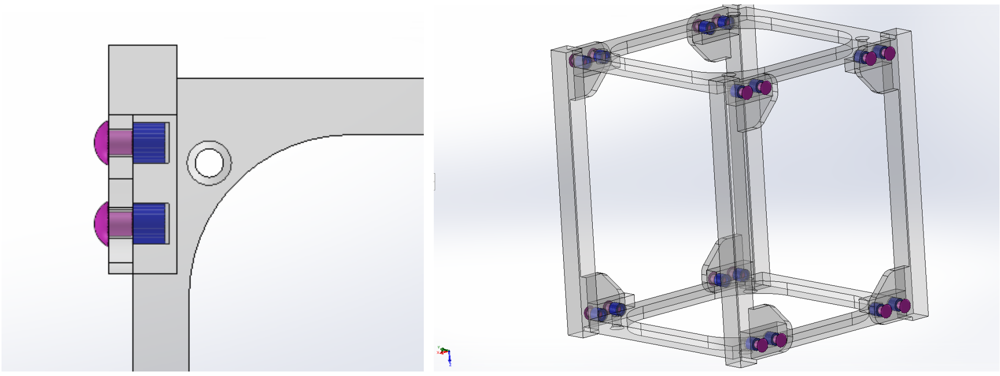

Figure 4.10: Modular design connection

The figure 4.11 shows the final assembly of the connected parts.

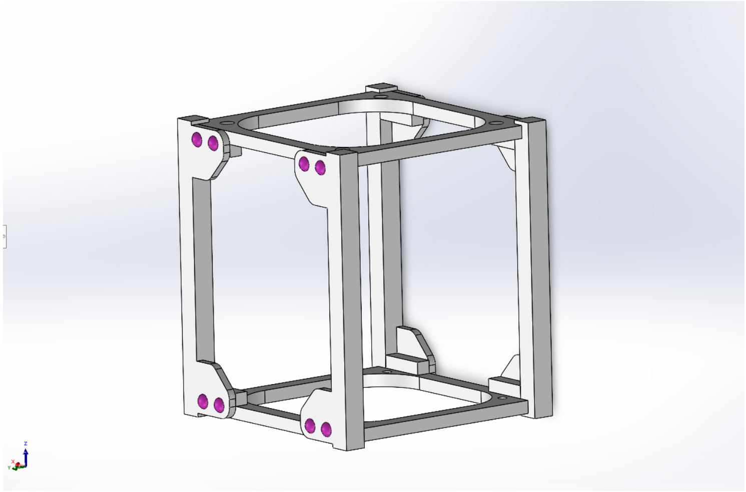

Figure 4.11: Second design assembly

4.5 Third Design

The third design was actually the first one to be finished. It's a two parts design like the first but it's divided in a different way. In this case there is one major part that comprehend five of the six faces of the cube and the other face is the closing one. The two parts are shown in figure 4.12 .

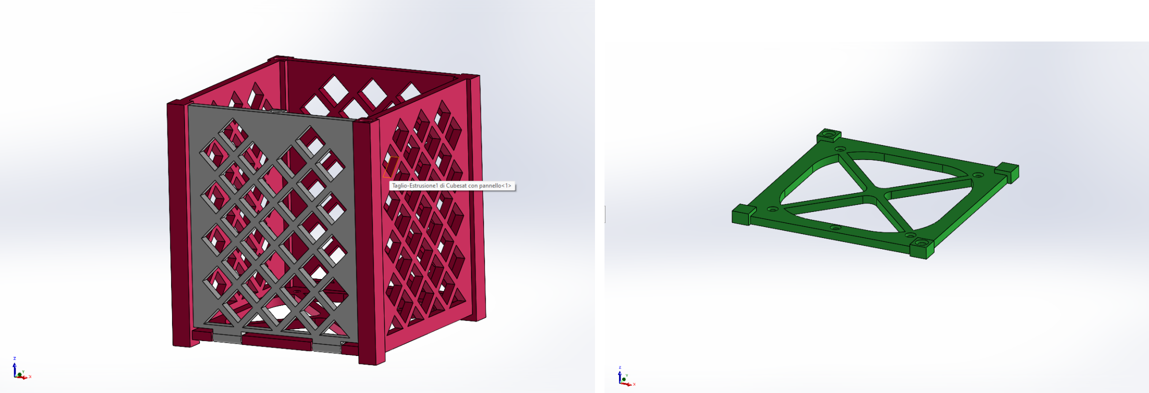

Figure 4.12: Third design parts

The first part is not a total monocoque, in fact, it has a face (the gray one in figure 4.12) that can open thanks to a hinge incorporated in the design. This is possible thanks to the freedom given by the AM process. A feature like that can't be manufactured by traditional manufacturing process.

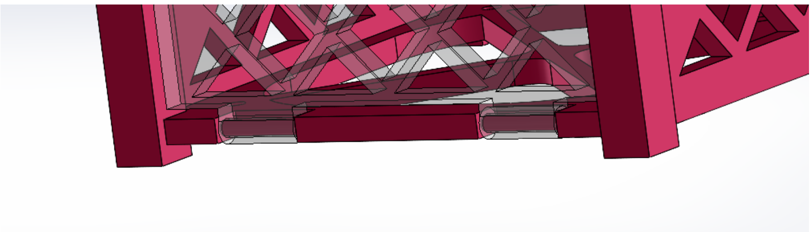

Figure 4.13: Hinge feature

The face that can open allow a faster way to work on the payload, if needed, even when it is already assembled completely inside the structure. This is an important feature that is required for any design.
As for the connecting parts needed for this design, they are much less than the second and more like the first. To connect the two parts, two screws are used on top of the rails and another one is used to block the hinged door in place. The finished result is shown in figure 4.14.
Even though this third design had everything that was needed, it was decided not to use it in the next phases of the project because printing the hinge with the machine in our possession wouldn't be feasible.

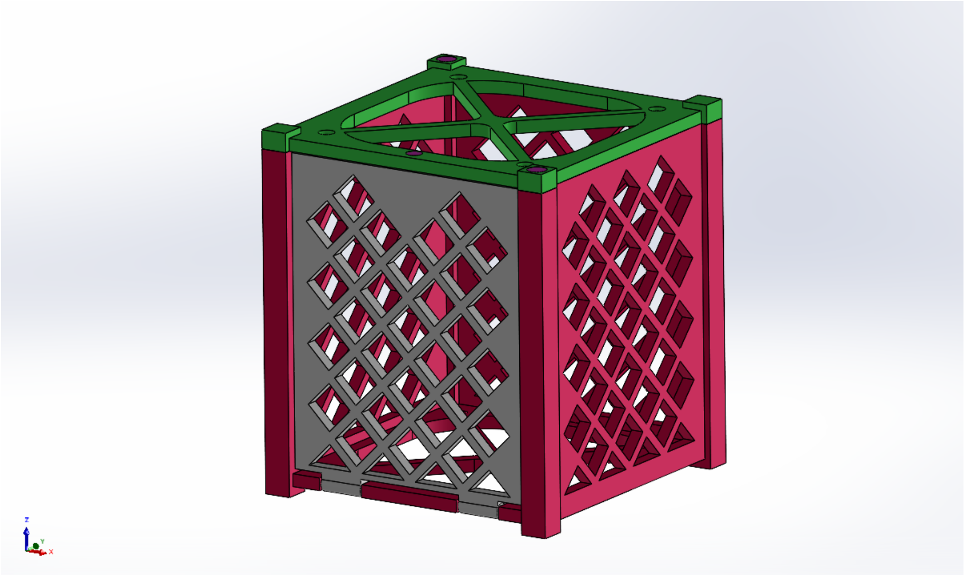

Figure 4.14: Third design

4.6 Payload Design

For the payload, the objective was to create something as similar to reality as possible in terms of mass and with the possibility to change something to create more scenarios. There was the possibility to recreate a 1:1 copy of some of the modules that would have been inside a CubeSat (like Matthew Napoli did in [10]), but printing it would have also mean that in terms of mass it would have been significantly lighter than the real one.
To contrast this difference a very simple module was created:

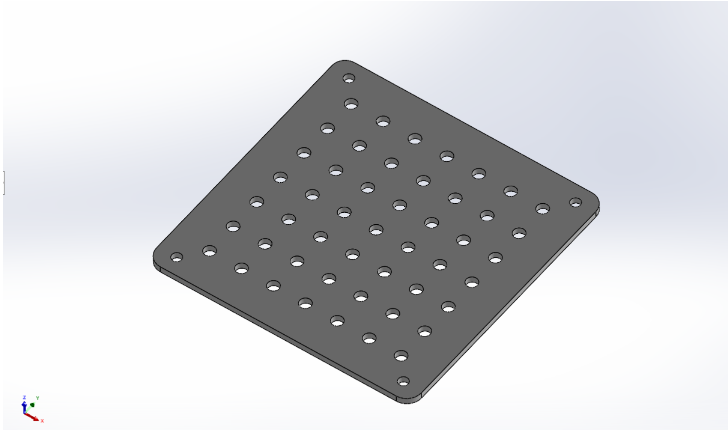

Figure 4.15: Payload Module

Each one of the hole can be filled with a small bolt that simulate the mass of a component, the sum of all the masses creates the one of the real module.
The payload it self is the sum of five of this module put together with off the shelf card spacers which can be also of different dimensions to create other payload design.
Obviously not all the parts inside a real CubeSat would be present but for the purpose of the project it was enough.

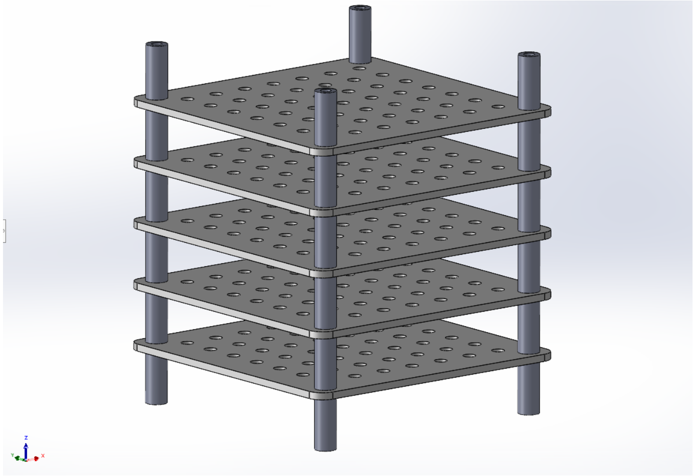

Figure 4.16: Payload complete

Chapter 5

Manufacturing Process

5.1 Process description

Being the parts produced by additive manufacturing, the process it self wasn't as straight forward as in traditional manufacturing, in fact, a lot of trial and error was used.

At first it was important to understand if the designs were printable and even more important was to examine if the various parts were compatible. To do both things a first print of both design was done using a different printer and in particular a different material, cheaper then PEEK, Onyx. This allowed to make mistakes without wasting material and have lower cost. This strategy brought to light some minor design flaws, in the structure it self, that were corrected. Also during this phase the connections between the parts and the inserts were checked. After all the parts were completed and updated when needed, the final printing using PEEK material was also brought to term after some issues with the printer itself.

5.2 3D Printers

Like it's said in the previous paragraph, two printers were used for the creation of both designs:

Markforged MARK 2 The MARK 2 it's a very precise and reliable 3D printer capable of printing Carbon Fiber Composites, like Onyx, thanks to it's hardened extrusion system.

Along with the usual FFF (Fused Filament Fabrication) features, the Mark Two is equipped with a second-generation fiber reinforcement system, allowing for the integration of continuous fiber into parts.

With a z axis resolution of 100 μm to 200 μm it can achieve a great level of finishing With it's working volume of 320 x 132 x 154 mm it was possible to print all the parts needed for both designs in only two sessions.

In the table 5.1 the printer's parameters used, on the markforged software Eiger, to achieve the end results are shown.

For the first design, it was chosen to use a gyroid infill, instead of the triangular, to fill better the space, particularly inside the walls where if the triangular infill had been used, hallow parts tall as much as the wall would have been present.

Table 5.1: MARK 2 parameters

Parameter	First Design	Second Design
Layer height	0.2 mm	0.2 mm
Fill pattern	Gyroid	Triangular
Fill density	40%	40%
Roof & Floor layers	4	4
Wall layers	4	4

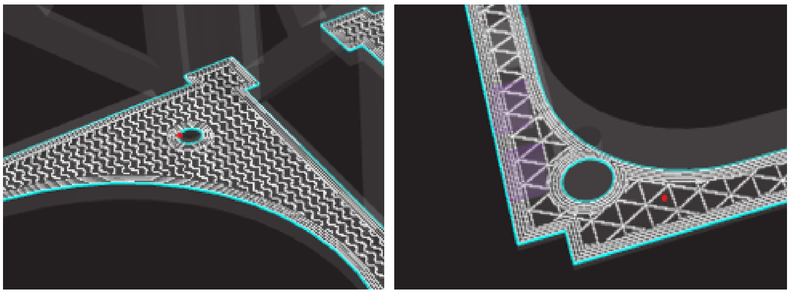

Figure 5.1: Infill patterns used: left gyroid and right triangular

APIUM 220 Printing PEEK is not an easy task, in particular the printer needs to have some characteristics:

- High extruder Temperature to properly melt the material:
- Heated build plate to ensure proper adhesion and reduce warping:
- Enclosed and heated chamber to minimize thermal stresses:
- Specialized nozzle
- High quality motion system

The APIUM 220, meet all the characteristics listed above and is capable of printing PEEK with solid results and reproducibility.
The printing volume is smaller than the MARK 2 being 205 x 155 x 150, this resulted in more printing sessions.
As for the slicer software UltiMaker CURA was utilized in this case setting the same parameters as the MARK 2 (table 5.1).To be able to achieve a better result for the first design in terms of shrinking and warping, a support like structure was added to the base shown in the picture below (orange circle in figure 5.2):

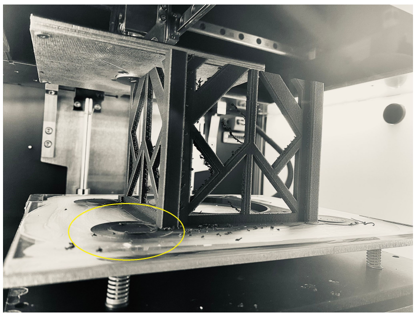

Figure 5.2: Apium 220 monolithic design printing session

5.3 Materials used

5.3.1 Onyx

Onyx is composites based material produced by Markforged. It's a nylon composite infused with micro carbon fibers, producing precise parts with an almost flawless surface finish. Its versatility is unmatched, offering high strength, toughness, and chemical resistance when printed on its own. Additionally, Onyx can be reinforced with Continuous Fibers to create parts with strength comparable to aluminum.[23]
In particular, for the production of the designs, the Onyx ESD was used. Onyx ESD meets the stringent ESD-safe requirements of top manufacturers while maintaining the industry-leading print quality of Onyx. It is stronger and stiffer than Onyx and features the same nearly flawless surface finish. This makes Onyx ESD ideal for advanced manufacturing applications, including electronics assembly, industrial robotics, and process automation. ESD materials for 3D printing are formulated with additives that impart electrical properties suitable for dissipating static charges. The table 5.2 shows the properties of the onix used.

Table 5.2: Onyx ESD properties[24]

Property	Value
Module of elasticity (Gpa)	4.2
Yield strength (MPa)	52
Tensile strength (MPa)	50
Elongation at break (%)	25
Flexural strength (MPa)	83
Flexural modulus (GPa)	3.7
Density (g/cm^3)	1.2

5.3.2 PEEK

PEEK is a member of the PAEK (Polyaryl Ether Ketone) polymer family, which includes polymers such as PEK, PEEK, PEEKK, PEKK, and PEKEKK. This family of polymers is renowned for its high-temperature stability and exceptional mechanical strength. Among these materials, PEEK is the most widely used for 3D printing and is produced in large quantities due to its metal-like machinability and versatile performance.
PEEK offers a unique blend of mechanical properties, including excellent chemical resistance, wear resistance, fatigue resistance, and low creep. It also features high-temperature stability, low flammability, and good dielectric properties.
For more demanding applications, neat PEEK might not always provide sufficient performance. In such cases, PEEK can be reinforced with various additives, such as carbon fibers or glass fibers, to enhance its properties. While virgin PEEK is colorless, carbon fiber-reinforced PEEK has a distinctive black appearance. Both the standard and reinforced forms of PEEK are employed across a wide range of industries for advanced engineering applications.[25]
The PEEK material used for the project is a reinforced carbon fiber PEEK with the properties shown in table 5.3.

Table 5.3: TEKAPEEK properties

Property	Value
Module of elasticity (Gpa)	6
Tensile strength (MPa)	112
Elongation at break (%)	10
Impact strenght (Charpy) (kJ/m^2)	92
Ball indentation hardness (MPa)	298
Density (g/cm^3)	1.38
Glass transition temperature (°C)	147
Melting temperature (°C)	341

These type of properties make PEEK a material usable in space projects.
The values listed in the table 5.3 are for a full infill print. having used a 40% infill, a proportion is needed in this case. For the type of project it was decided not to characterize the material, being also fully aware that this choice will create some discrepancies between the FEM model and experimental data.

5.4 Printed models

5.4.1 Masses

In the introduction was reported that on average an aluminum structure weight around 120g which is already lightweight, from this starting point the masses of the PEEK printed structures are shown in the table 5.6 and 5.5. Also the total masses shown are considering the connections (insert and screws).

Table 5.4: Monolithic Design weight table

Monolithic	
Part	Weight
Part 1	60 g
Part 2	56 g
Feet	2 g
Total	125.8 g

Table 5.5: Classic Design weight table

Classic	
Part	Weight
Plate	15 g
Rail	10 g
Total	73 g

From the tables 5.6 and 5.5 it is possible to see how the monolithic design is much heavier than the classic one, but this was expected. It is important to note that the

weight in the classic design is almost half of the aluminum counterpart.
The payload for now will be considered empty, without any additional weight of washers or screws. Those could bring the maximum payload mass to around 250g.

Table 5.6: Payload Design weight table

Payload	
Part	Weight
Plate	13 g
Nylon parts	0.5 g
Total	82.7

5.4.2 Dimensions

In terms of dimensions the CubeSats measures are shown in table 5.7.

Table 5.7: CubeSats dimension

Dimension	Classic	Monolithic	Correct
x	10.1 cm	10.17 cm	10.00 cm
y	10.07 cm	10.15 cm	10.00 cm
z	11.45 cm	11.41 cm	11.35 cm

The dimensions are slightly out of the tolerances in all directions. In a real mission scenario, interferences with the deployer could occur. This problem can be avoided by predicting this phenomenon and scaling down the design by a small factor so that the finished product is compatible with the design specifications.

5.4.3 Finished CubeSats

Finally the complete assembled parts shown in figure 5.3.

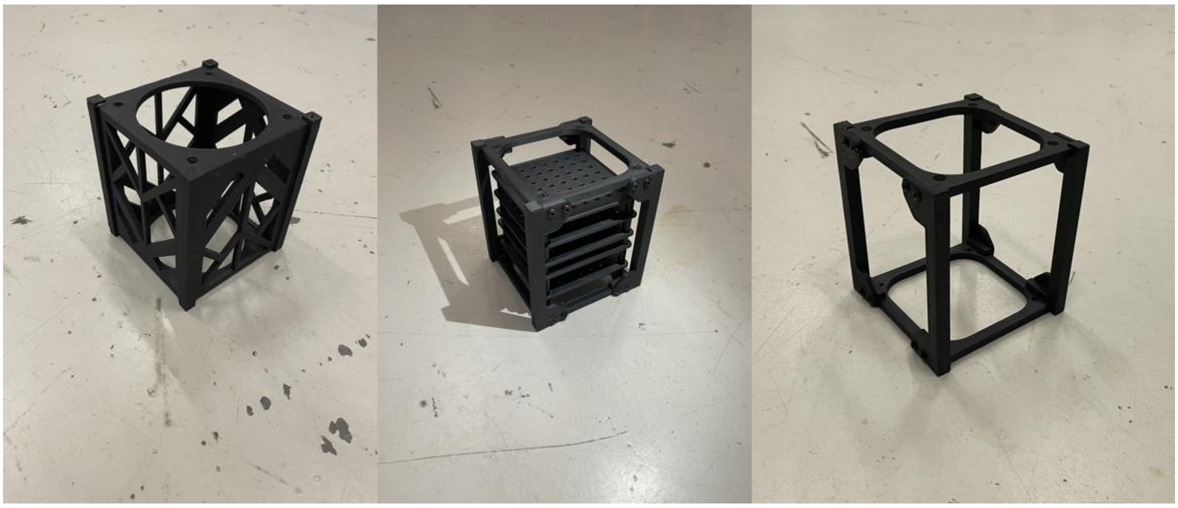

Figure 5.3: Assembled printed structures

Chapter 6

Structures Modal Analysis

6.1 Introduction

Over the present chapter, all the steps of a modal analysis on both the structures will be explained. The goal of the modal analysis is to characterize the structures, finding the natural frequencies and mode shapes, both using the FEM models and a physical impact test before doing a correlation between them to find how close they are to each other.
A simplified procedure is shown in figure 6.1 and, as it can be seen, mainly two software were used:

- Simcenter 3D for the creation of the FEM models starting from the CAD models seen in chapter 4.
- Simcenter TestLab and in this particular case the Impact Testing module and Modal Analysis module, for the acquisition and analysis of the experimental data.

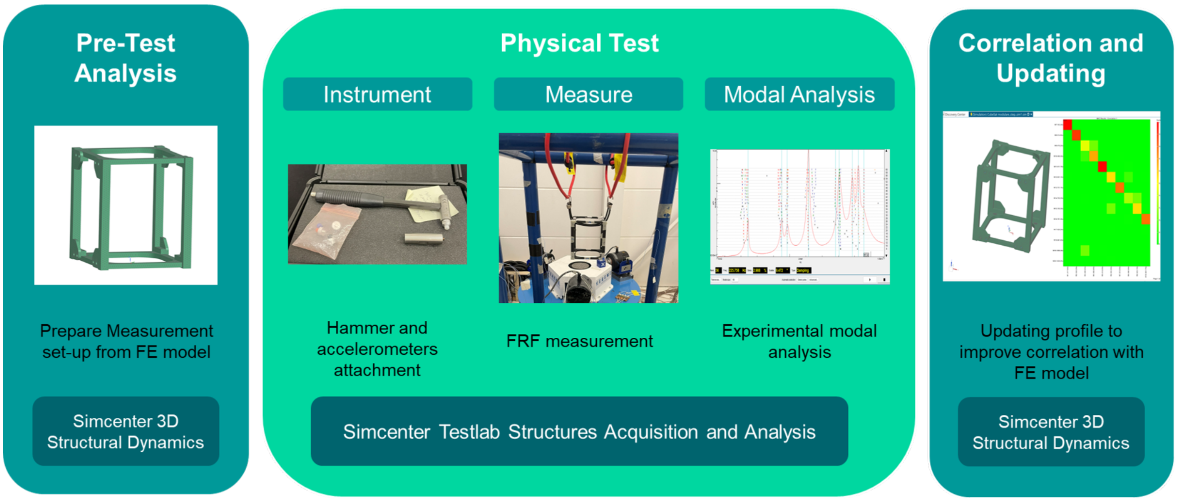

Figure 6.1: Modal survey procedure

6.2 FEM models and Pre-Test Analysis

The FEM models of both structures were created starting from the CAD models and importing them into Simcenter 3D. Being the FEM not the focus of the thesis, they were created with some assumptions that are going to be explained in this section.

6.2.1 Material

The material of both structures is PEEK and it was created in Simcenter 3D using the properties listed in the table 5.3.
This was the starting point and the first thing that was changed was the density because, being the parts printed with 40 % infill, to achieve a correlation of masses between the part and the FEM the only parameter usable was the density.
To be able to correlate the mass, the density was lowered from 1.38 g/cm^3 to 0.89 g/cm^3. In terms of Module of Elasticity it needed to be lowered too because if not the frequencies would have been too high with respect to the experimental data. In particular, the optimal values were found after the first physical test.
The values that better approximated the experimental results were the one shown in table 6.1

Table 6.1: Values of E for the FEM in both structures

Design	E
Monolithic	3500 Mpa
Classic	4500 Mpa

The difference between the material characteristics between the two structures is possible because of how they have been printed but they are still also an approximation because no physical test have been done on the material at this moment.
The biggest approximation in terms of material was also to consider it an isotropic material so no meso-structure of the material was taken into consideration.

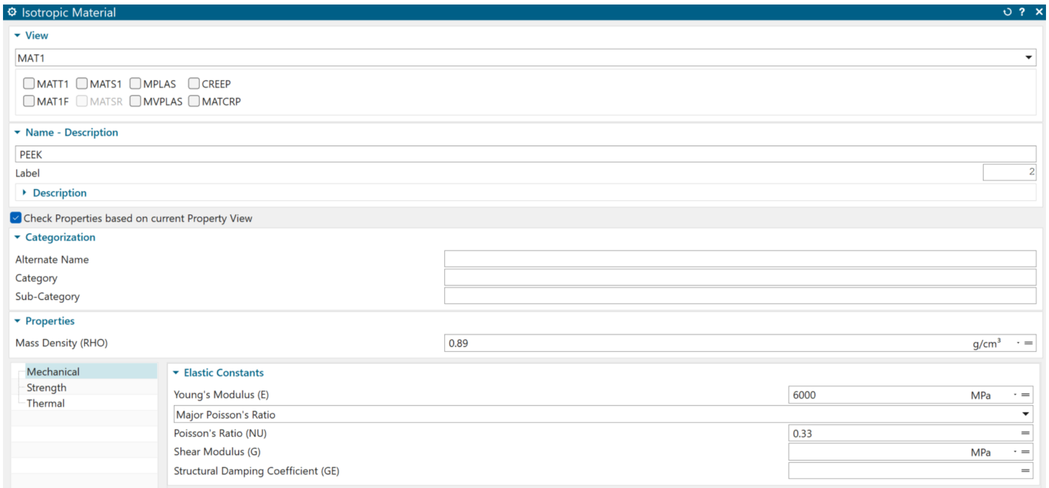

Isotropic Material

View

MAT1

☐ MATT1 ☐ MATS1 ☐ MPLAS ☐ CREEP
☐ MAT1F ☐ MATSR ☐ MVPLAS ☐ MATCRP

Name - Description

PEEK

Label: 2

Description

☑ Check Properties based on current Property View

Categorization

Alternate Name:
Category:
Sub-Category:

Properties

Mass Density (RHO): 0.89 g/cm³

Elastic Constants

Young's Modulus (E): 6000 MPa
Major Poisson's Ratio
Poisson's Ratio (NU): 0.33
Shear Modulus (G): MPa
Structural Damping Coefficient (GE):

Figure 6.2: Material definition in Simcenter 3D

6.2.2 Solid mesh

For both structures the mesh itself have been chosen to be a CTETRA type of 3D mesh. In both cases a mesh convergence study have been done to find the adequate compromise between the computational cost and the quality of the results (figure 6.3).

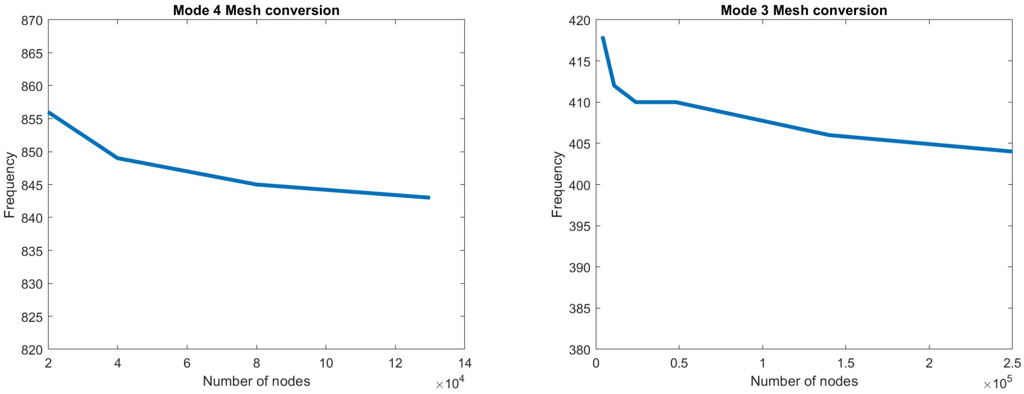

Figure 6.3: Monolithic Design (left) and Classic Design (right) convergence study

After the convergence study was finished, it was decided for each design a number of nodes and in particular the values in table 6.2

Table 6.2: Number of nodes for the 3D mesh of the structures

Design	Nodes
Monolithic	63689
Classic	39419

6.2.3 Monolithic Design Connections

The Monolithic design brings, within itself, different connections feature that aren't simple to model. It has glued parts on the top and bottom faces, a triangular rail type of connection between the 2 bigger part and 4 insert-screw connections. To model these types of connections different feature have been used:

- Glued parts: these were the easiest to model, in fact, it was achieved by using a command inside the Simcenter 3D software called Face to Face Gluing (yellow cones in figure 6.5).
- Triangular rail: after a lot of trial and error the solution to this problem was to simply create a mesh mate connection between the parts. The mesh mating connect the 2 bodies and the associated 3D mesh, this way it moves as 1 part in those points. In any of the other cases the faces would flap at a resonance frequency much lower than the correct one. This was the exact reason it was created the triangular feature, to stop those exact faces to flap, so this solution, as approximated as it is represent the model better.
- Insert-screw connection: the best way found to model these connections was to use a 'Bolt in a tapped hole' type of 1D connection (figure 6.4). Here the edge

where the screw enters the first part and the surface that would be the thread of the insert are chosen. A CBAR element is created between the center of the first hole and the center of the cylindrical surface of the thread and it also creates RBE2 elements to connect the different nodes to the center nodes.
The CBAR element is going to be a ROD with the diameter of the screw M3 and as material Aluminum 5086 is going to be used.

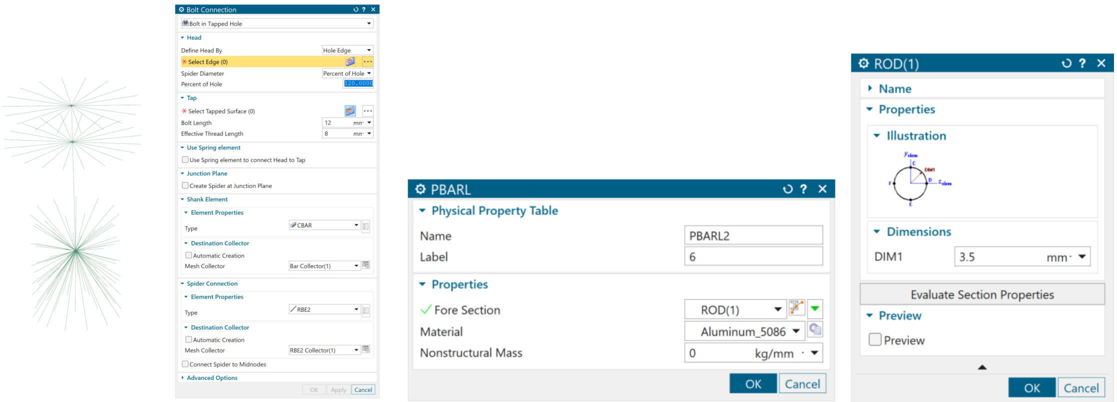

Bolt Connection
Bolt in Tapped Hole
Head
Define Head By: Hole Edge
Select Edge (0)
Spider Diameter: Percent of Hole
Percent of Hole: 120.0000
Tap
Select Tapped Surface (0)
Bolt Length: 12 mm
Effective Thread Length: 8 mm
Use Spring element
☐ Use Spring element to connect Head to Tap
Junction Plane
☐ Create Spider at Junction Plane
Shank Element
Element Properties
Type: CBAR
Destination Collector
☐ Automatic Creation
Mesh Collector: Bar Collector(1)
Spider Connection
Element Properties
Type: RBE2
Destination Collector
☐ Automatic Creation
Mesh Collector: RBE2 Collector(1)
☐ Connect Spider to Midnodes
Advanced Options

PBARL
Physical Property Table
Name: PBARL2
Label: 6
Properties
Fore Section: ROD(1)
Material: Aluminum_5086
Nonstructural Mass: 0 kg/mm

ROD(1)
Name
Properties
Illustration
Dimensions
DIM1: 3.5 mm
Evaluate Section Properties
Preview
☐ Preview

Figure 6.4: FEM model of Monolithic Design connections

After all of the connection and the 3D mesh were applied the FEM model was completed (figure 6.5).

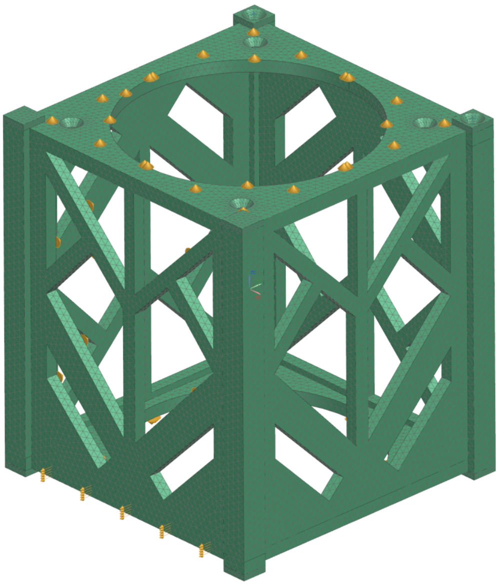

Figure 6.5: FEM model of the Monolithic Structure

6.2.4 Classic Design Connections

The classic design is a simpler design in general and for the connection it uses only one type, the insert-screw. These connections have been modeled using the same approach as in the Monolithic design but with small changes. For example the dimensions of the screw it self has changed, but most importantly the element type between the spiders have been changed to a more rigid one RBE2 (figure 6.6). This was done because the importance of the connection rigidity, compared to the material one, in this case was higher because of the lighter weight and the number of pieces. The completed FEM is shown in figure 6.7

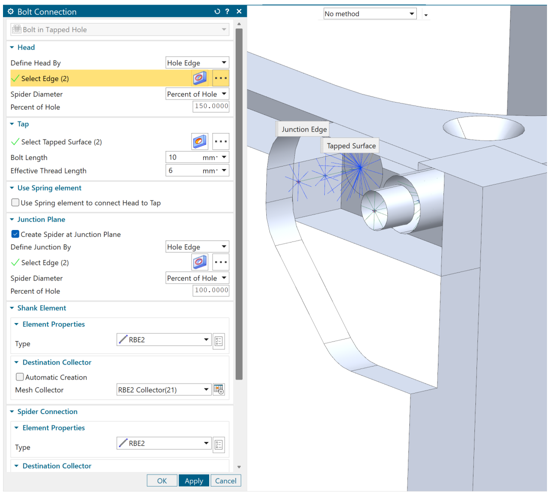
Bolt Connection

Bolt in Tapped Hole

Head

Define Head By: Hole Edge

✓ Select Edge (2)

Spider Diameter: Percent of Hole

Percent of Hole: 150.0000

Tap

✓ Select Tapped Surface (2)

Bolt Length: 10 mm

Effective Thread Length: 6 mm

Use Spring element

☐ Use Spring element to connect Head to Tap

Junction Plane

☑ Create Spider at Junction Plane

Define Junction By: Hole Edge

✓ Select Edge (2)

Spider Diameter: Percent of Hole

Percent of Hole: 100.0000

Shank Element

Element Properties

Type: RBE2

Destination Collector

☐ Automatic Creation

Mesh Collector: RBE2 Collector(21)

Spider Connection

Element Properties

Type: RBE2

Destination Collector

Figure 6.6: FEM model of Classic Design connections

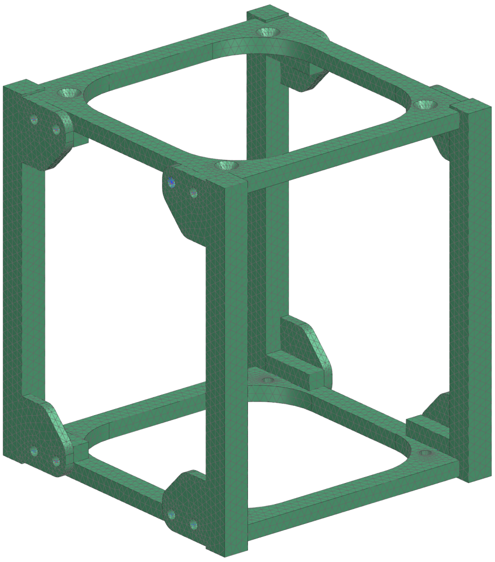

Figure 6.7: FEM model of Classic Design

6.2.5 FEM Results

Using the Solution 103 of NX Nastran, the natural frequencies and the mode shapes of the structures were identified. The results are listed in table 6.3.

Table 6.3: FEM natural frequencies

Mode	Monolithic [Hz]	Classic (E=3500 Mpa) [Hz]	Classic (E=4500 Mpa) [Hz]
1	576	205	232
2	631	210	238
3	748	396	449
4	860	407	462
5	903	416	472
6	919	563	638
7	944	598	679
8	979	613	695
9	1010	634	718
10	1053	638	723
11	1086	802	909
12	1013	880	998

From this table it's possible to extrapolate some information: being the monolithic structure a heavier one, almost double the weight as the classic one, the first natural frequency should occur at a much higher frequency. Most of the modes in the monolithic design are in the range between 900 and 1100 Hz, that is because those are linked to local modes of the faces of the structure (see figure 6.8). For the classic design it is possible to see the effect of the change in the material but also the frequencies are more distributed in the frequency range.

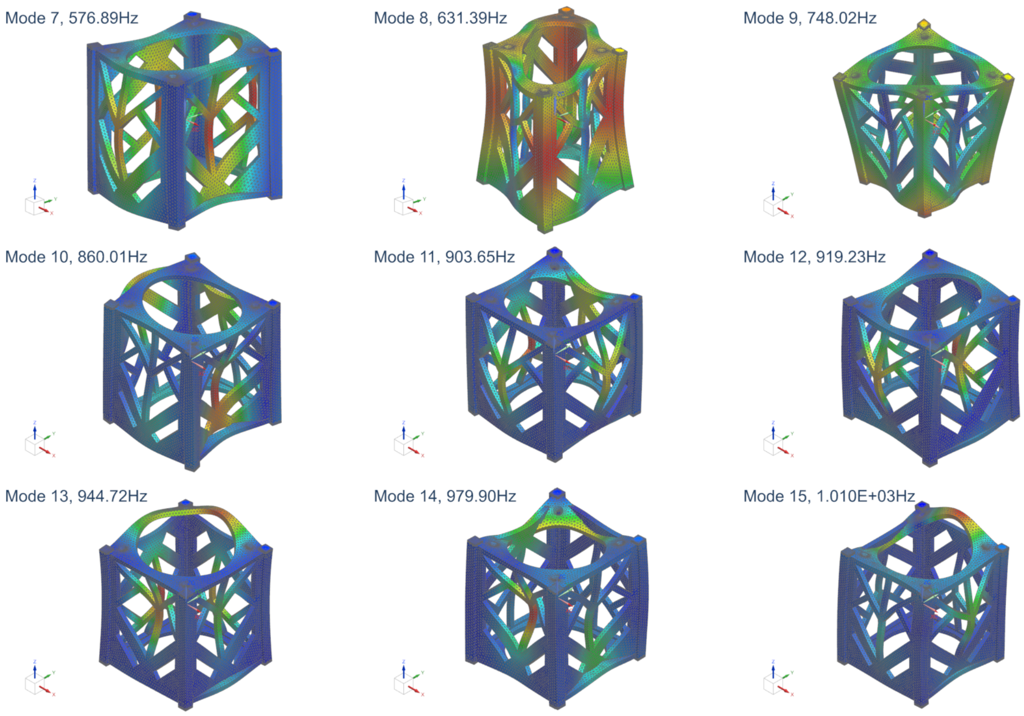

Figure 6.8: First 9 modes of Monolithic structure

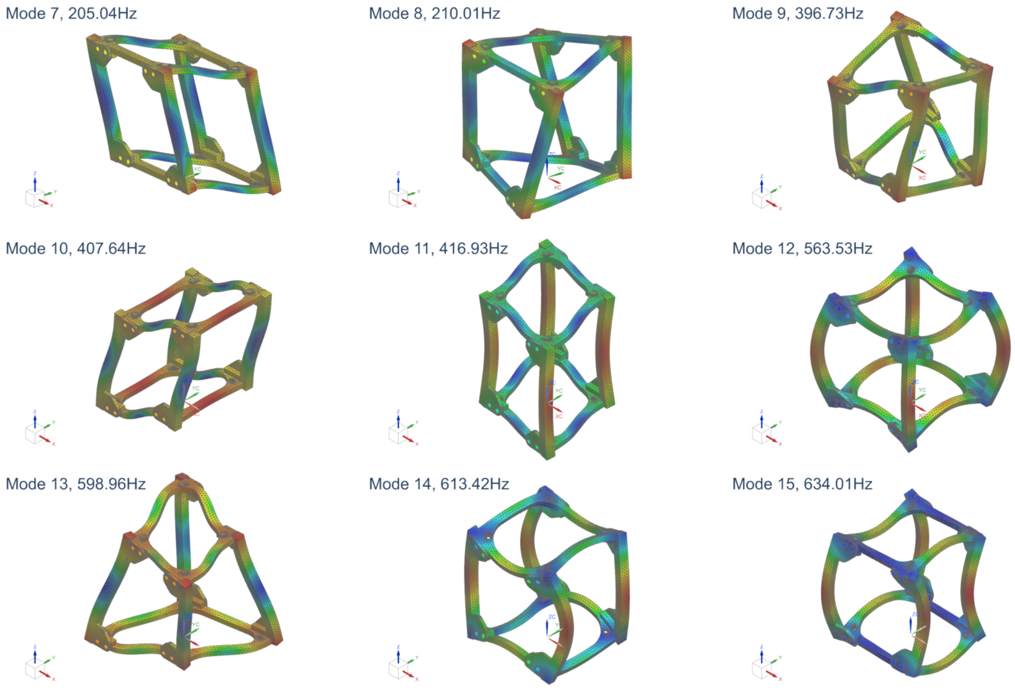

Figure 6.9: First 9 modes of Classic structure

6.3 Physical Test

6.3.1 Set-up

The logic behind hammer testing and the basic set-up have been explained in section 3.1.3. Following those steps a more detailed analysis and explanation about the set-up used in this case is needed.
First let's start with the components used: the PC on which Simcenter Testlab is installed is connected to a Simcenter SCADAS via Ethernet connection. A SCADAS (Structural Condition and Data Acquisition System) is a comprehensive system designed to collect, process, and analyze data from various sensors and instruments. The SCADAS used has 80 channel to which the accelerometers and the hammer are connected. All the tests were done using 4 uniaxial accelerometers, attached to the structure using bee wax, and one hammer (figure 6.10).

The choice of the hammer's tip, as explained before, is really important. In this case after different tests using the bandwidth and the quality of the response as parameters, the best tip to use with PEEK was found to be the hard plastic tip. Analyzing the bandwidth survey is already possible to see why (figure 6.11). The goal in the bandwidth is to achieve the highest frequency before the signal drop by 10 dB. The rubber tip don't even get to 500Hz which is too low anyway. The hard plastic and the metallic, instead, both go over 1400 Hz. Even tho the metallic reach a slightly higher frequency it was found that it brought much more frequently the sensors to overload, so it was dropped.

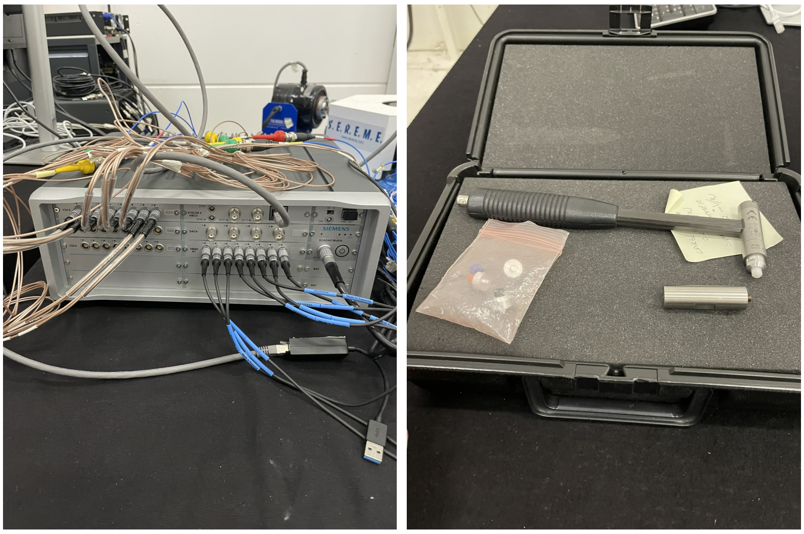

Figure 6.10: SCADAS (left) and Hammer (right) used

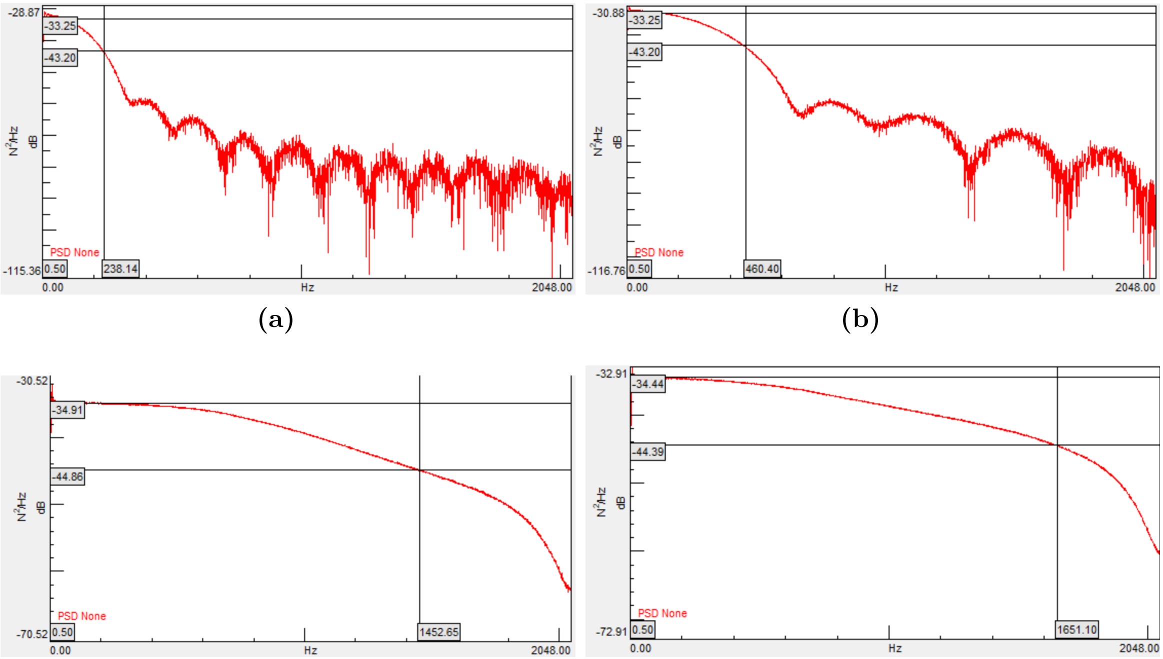

(a) (b)

(c) (d)

Figure 6.11: (a) Rubber , (b) hard rubber, (c) Hard plastic and (d) Metallic tip

Another very important factor to take into consideration when doing hammer testing, as already discussed, are the boundary conditions. In this case the goal was to recreate the free-free condition used also in the FEM models. To do that a combination of soft spring ropes were used to suspend the structure (figure 6.12).

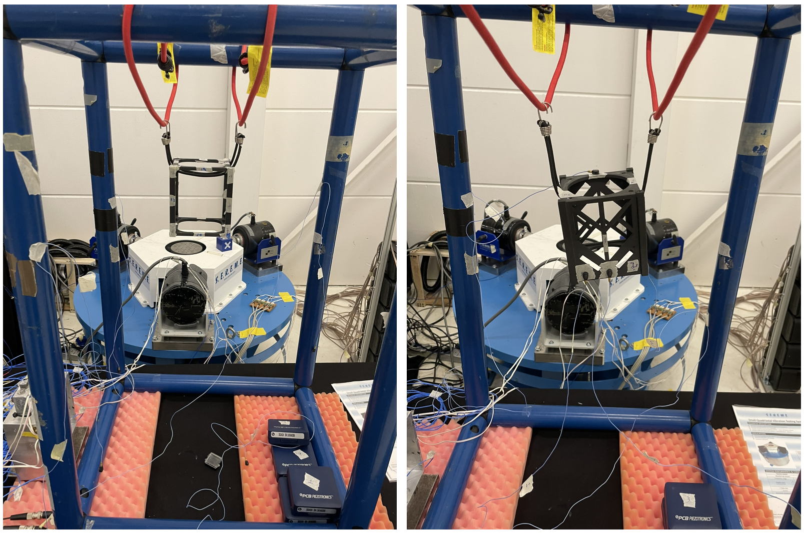

Figure 6.12: Boundary conditions

After the conditions and the equipment were defined 2 different strategies have been used to get the data needed:

- **Roving accelerometers**: during this type of tests, if the number of response needed is higher than the number of accelerometers, after hitting in the required points, the accelerometers need to moved to the next positions. So, for example in the case of both structures, at least 12 responses were required and only 4 accelerometers were available. In both cases the tests were divided into 3 sections, each of them had the same hitting points but the responses were measured in different positions. This division brings out some problems in the FRFs analysis because of the changes in the mass positioning but also is more complex and require a change of physical set-up, channel set-up also, every section. The geometry created with 12 points is also very simple and don't recreate in a good way the real structure so it may be that in the correlation part there seems to be a good correlation between the FEM and the structure but in reality is good only in those 12 points and some modes could be lost.

- **Roving hammer**: during this test, as compared to the roving accelerometers, the set-up stays the same during the test in fact, the accelerometers are placed in the fixed positions and is the hammer that moves in this case. The structure is hit in a higher number of points (more than 40 in both structures) and the responses FRFs are taken by the accelerometers. After the test is completed, to be able to see the response in all the points we hit, the FRFs matrix needs to be switched so that the hitting points become the response and the accelerometers becomes the hit. This leads to a better result in terms of geometry and mode shapes but also the FRF are cleaner.

6.3.2 Experimental results

Both the structures were tested with different setups with the roving accelerometer technique and once with the roving hammer technique. After the measures were complete the PolyMax algorithm, available in Simcenter Testlab, was used first to find the poles and then compute the mode shapes.

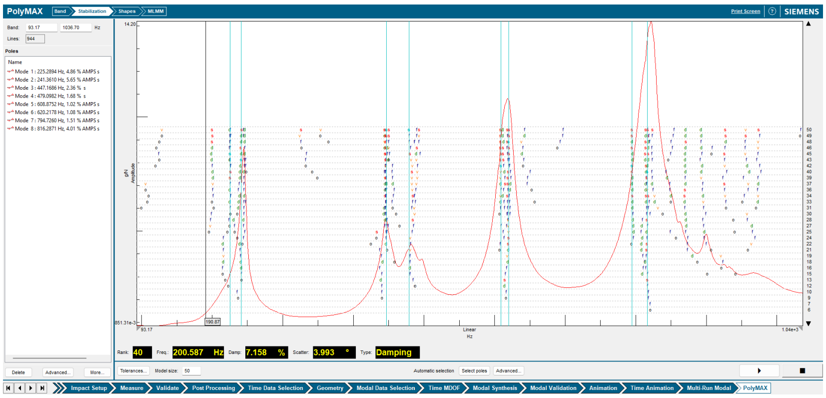

Band: 93.17 1036.70 Hz
Lines: 944

Mode 1 : 225.2894 Hz, 4.86 % AMPS s
Mode 2 : 241.3610 Hz, 5.65 % AMPS s
Mode 3 : 447.1686 Hz, 2.36 % s
Mode 4 : 479.0982 Hz, 1.68 % s
Mode 5 : 608.8752 Hz, 1.02 % AMPS s
Mode 6 : 620.2178 Hz, 1.08 % AMPS s
Mode 7 : 794.7260 Hz, 1.51 % AMPS s
Mode 8 : 816.2871 Hz, 4.01 % AMPS s

Rank: 40 Freq.: 200.587 Hz Damp: 7.158 % Scatter: 3.993 ° Type: Damping
Model size: 50

(a)

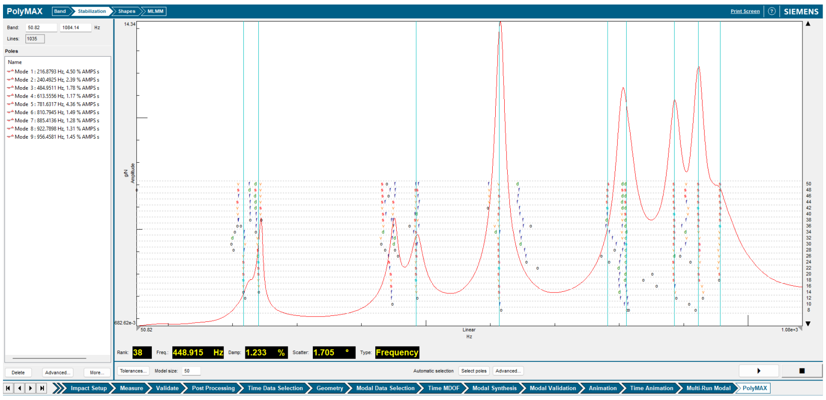

Band: 50.82 1084.14 Hz
Lines: 1035

Mode 1 : 216.8793 Hz, 4.50 % AMPS s
Mode 2 : 240.4925 Hz, 2.39 % AMPS s
Mode 3 : 484.9511 Hz, 1.78 % AMPS s
Mode 4 : 613.5556 Hz, 1.17 % AMPS s
Mode 5 : 781.6317 Hz, 4.36 % AMPS s
Mode 6 : 810.7945 Hz, 1.49 % AMPS s
Mode 7 : 885.4136 Hz, 1.28 % AMPS s
Mode 8 : 922.7898 Hz, 1.31 % AMPS s
Mode 9 : 956.4581 Hz, 1.45 % AMPS s

Rank: 38 Freq.: 448.915 Hz Damp: 1.233 % Scatter: 1.705 ° Type: Frequency
Model size: 50

(b)

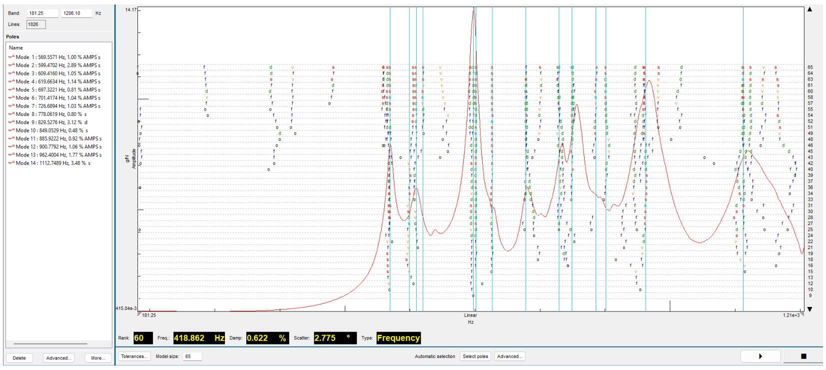

Band: 181.25 1206.10 Hz
Lines: 1026

Mode 1 : 569.5571 Hz, 1.00 % AMPS s
Mode 2 : 599.4702 Hz, 2.89 % AMPS s
Mode 3 : 609.4160 Hz, 1.05 % AMPS s
Mode 4 : 619.6634 Hz, 1.14 % AMPS s
Mode 5 : 697.3221 Hz, 0.81 % AMPS s
Mode 6 : 701.4174 Hz, 1.04 % AMPS s
Mode 7 : 726.6894 Hz, 1.03 % AMPS s
Mode 8 : 778.0619 Hz, 0.80 % s
Mode 9 : 829.5276 Hz, 3.12 % d
Mode 10 : 849.0529 Hz, 0.48 % s
Mode 11 : 885.9222 Hz, 0.92 % AMPS s
Mode 12 : 900.7792 Hz, 1.06 % AMPS s
Mode 13 : 962.4004 Hz, 1.77 % AMPS s
Mode 14 : 1112.7489 Hz, 3.48 % s

Rank: 60 Freq.: 418.862 Hz Damp: 0.622 % Scatter: 2.775 ° Type: Frequency
Model size: 65

(c)

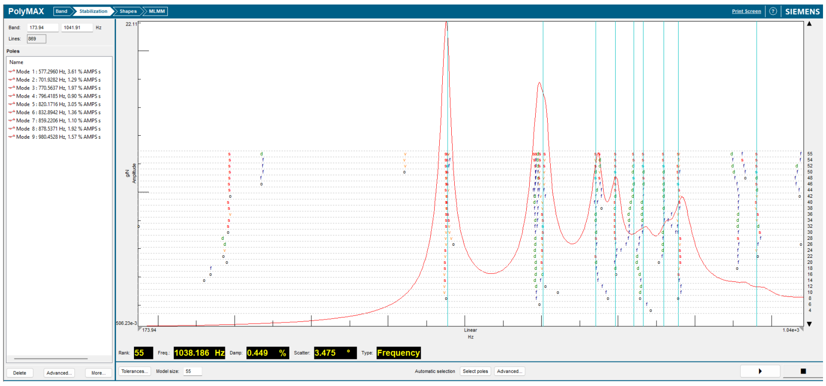

Band: 173.94 1041.91 Hz
Lines: 869

Mode 1 : 577.2960 Hz, 3.61 % AMPS s
Mode 2 : 701.9282 Hz, 1.29 % AMPS s
Mode 3 : 770.5637 Hz, 1.97 % AMPS s
Mode 4 : 796.4185 Hz, 0.90 % AMPS s
Mode 5 : 820.1716 Hz, 3.05 % AMPS s
Mode 6 : 832.8942 Hz, 1.36 % AMPS s
Mode 7 : 859.2206 Hz, 1.10 % AMPS s
Mode 8 : 878.5371 Hz, 1.92 % AMPS s
Mode 9 : 980.4528 Hz, 1.57 % AMPS s

Rank: 55 Freq.: 1038.186 Hz Damp: 0.449 % Scatter: 3.475 ° Type: Frequency
Model size: 55

(d)

Figure 6.13: a) Classic RA , b) Classic RH, c) Monolithic RA, d) Monolithic RH

From the stabilization diagrams in figure 6.13 it is possible to see how the monolithic design, as expected, being heavier and having less connections, have a first mode frequency much higher than the classic design. That being said it has also many more modes in general, as seen in the FEM models, due to the presence of the faces of the CubeSat.
In the diagrams is also possible to understand why the RH was a much better choice in terms of technique to use. In fact, the poles are much cleaner and there is no overlap between stable poles as in the RA case. This is due to the changing of the position of the accelerometers during the RA process which causes a small shift if the mode frequencies between each hitting section. The fact that the poles are much cleaner will result also in better mode shapes and better correlation in the end.

6.4 Correlation

After both the FEM models and the experimental models were completed, using the correlation module in Simcenter 3D was possible to correlate the mode shapes between the two models.
To do that it is important to define what is the metric that is going to be used to quantify this mode shapes correlation, the Modal Assurance Criterion (MAC).

$$MAC_{i,j} = \frac{|\phi_{Ai}^T \cdot \phi_{Bj}|^2}{\phi_{Ai}^T \cdot \phi_{Ai} \cdot \phi_{Bj} \cdot \phi_{Bj}^T} \tag{6.1}$$

where in the cases of this thesis ϕ_{Ai} is the i-th mode of the FEM model and ϕ_{BJ} is the j-th mode of the experimental data.
Each term of the MAC matrix (MAC_{ij}) is a scalar ranging from 0 to 1. Values close to 0 indicate a poor match between two modes. Conversely, values close to 1 indicate good correlation.

6.4.1 Classic Design: correlation

The lighter weight of the structure and simplicity of the connection reflects in a already decent correlation in the RA (figure 6.14 and table 6.4) case but is the RH (figure 6.15 and table 6.5) case that has an almost perfect result in terms of mode shape correlation thanks to a more defined geometry. The lower MAC number in some of the diagonal terms are possibly caused by the difference in hitting power by the operator resulting in lower acceleration response in some points and consequently in small difference in mode shape.
In terms of frequency difference between the models, is caused predominantly by the not correct characterization of the material. Also changing the E to get a complete 0% error at the first frequency would not get a much better result at higher frequency.

Table 6.4: Classic RA: correlation details

Pair	Exp. Mode	Frequency	FEM mode	Frequency	MAC	Freq.error
1	1	208.8	1	232.5	0.769	11.32 %
2	2	243.2	2	238.1	0.921	-2.09%
3	3	443	4	462.2	0.623	4.33%
4	5	609.3	12	998.8	0.716	63.93%
5	8	818.6	14	1142	0.646	39.51%

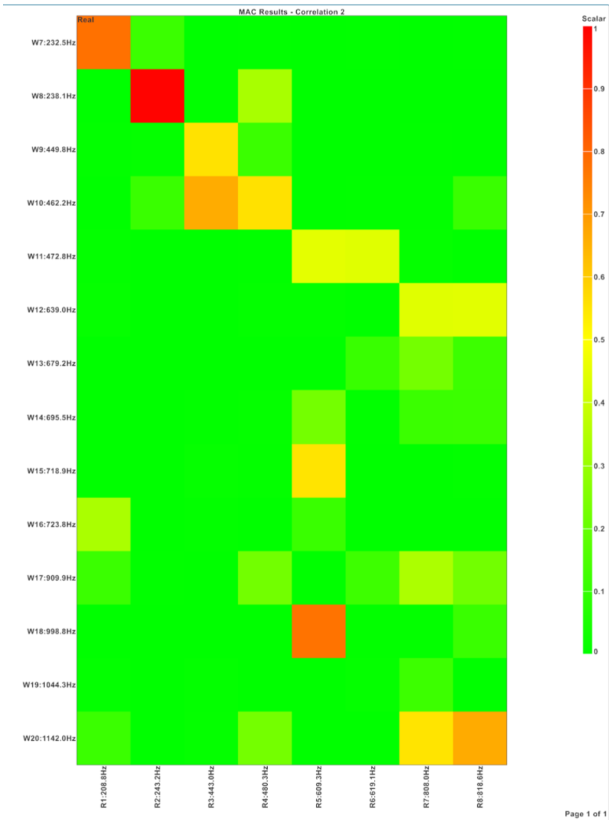

Figure 6.14: Classic RA MAC

Table 6.5: Classic RH: correlation details

Pair	Exp. Mode	Frequency	FEM Mode	Frequency	MAC	Freq. Error (%)
1	1	217.6	1	205.0	0.906	-5.78%
2	2	242.2	2	210.0	0.881	-13.3%
3	3	448.6	3	396.7	0.487	-11.56%
4	4	485.6	4	407.6	0.651	-16.05%
5	5	614.8	5	416.9	0.936	-31.18%
6	6	803.9	6	563.5	0.537	-29.87%
7	7	813.0	7	599.0	0.737	-26.32%
8	9	923.0	9	613.4	0.557	-33.54%
9	10	961.7	10	638.4	0.748	-33.62%

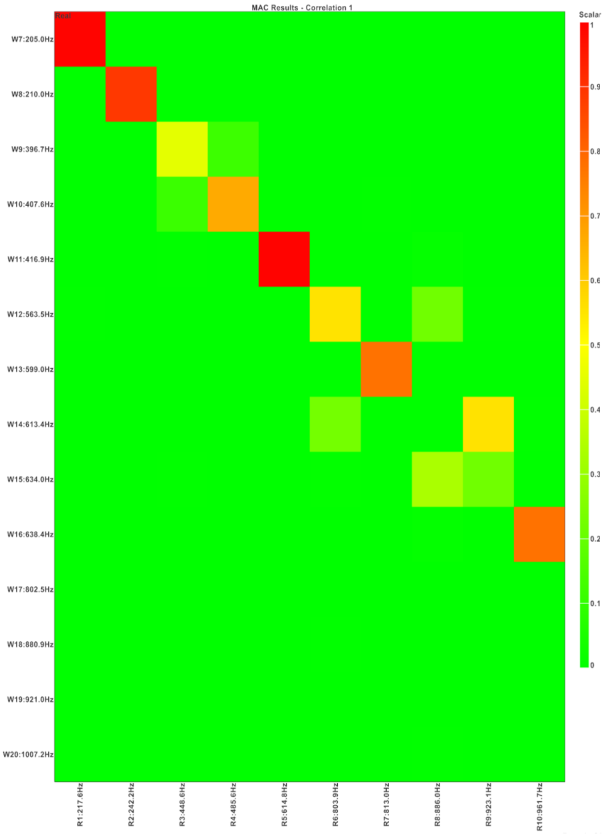

Figure 6.15: Classic RH MAC

6.4.2 Monolithic Design: correlation

In the monolithic case, having a lot of modes associated withe the faces, but most importantly not having a FEM model that represent the real connections (triangular connections) and the correct material reflect in poor correlation in general between the models. Only some modes are similar but the MAC is not diagonal meaning that adjustment needs to be made.

Table 6.6: Monolithic RA: correlation details

Pair	Exp. Mode	Frequency	FEM Mode	Frequency	MAC	Freq. Error (%)
1	1	568.5	4	860.0	0.513	51.27%
2	2	606.5	1	576.9	0.451	-4.89%
3	5	726.5	6	919.2	0.636	26.54%
4	10	951.3	5	903.6	0.422	-5.01%
5	12	1113.0	14	1191.0	0.797	6.96%
6	14	1325.0	12	1175.0	0.431	-11.34%

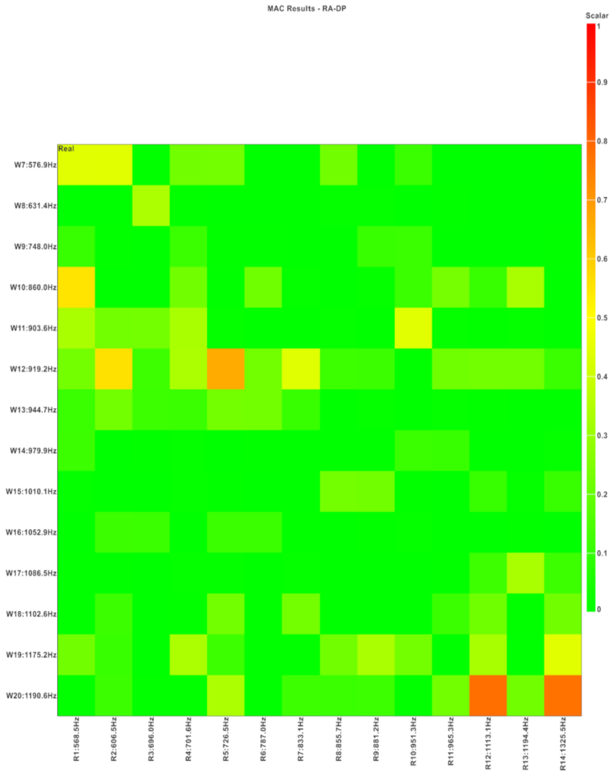

Figure 6.16: Monolithic RA MAC

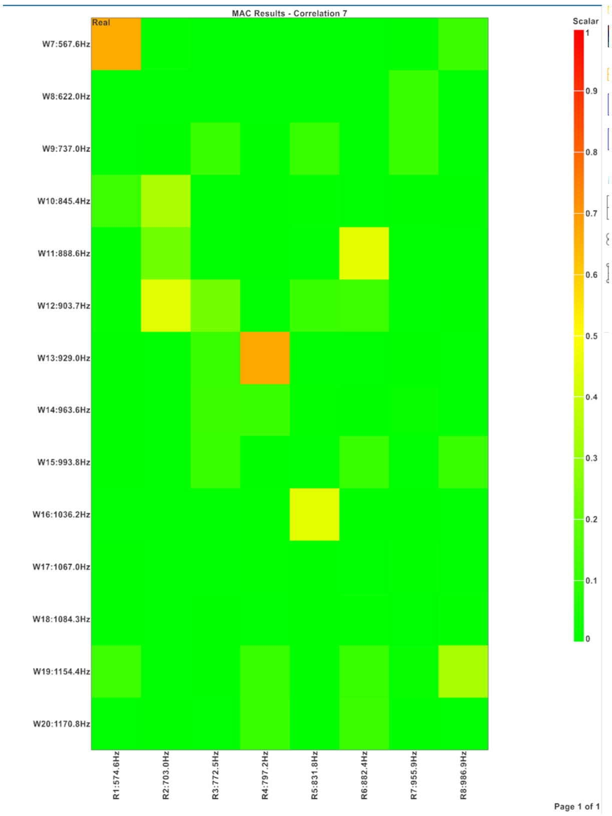

Figure 6.17: Monolithic RH MAC

Table 6.7: Monolithic RH: correlation details

Pair	Exp. Mode	Frequency	FEM Mode	Frequency	MAC	Freq. Error (%)
1	1	574.1	1	576.9	0.628	0.49%
2	2	701.8	6	919.2	0.424	30.98%
3	4	796.5	7	944.7	0.659	18.62%
4	5	831.5	10	1053.0	0.478	26.63%
5	6	880.1	5	903.6	0.471	2.68%

6.5 Classic design with payload

6.5.1 FEM model

After both the structure were modelled and tested, one was chosen to be tested also with the payload. In this case the Classic design was chosen thanks to the better results in terms of correlation between the FEM and the experimental data as it is shown in section 6.4.
For the FEM the same model of the structure was used in term of connections and materials. The difficult part was to model the payload. Various approach could have been used from a more accentuated approximation using only 1D and 2D elements to the one that was used in this case.
The approach was to use only 3D elements even in this case for all the parts, this made it simpler and faster to model.
The model was created using these steps:

- The four pillars that in reality are a stack of card spacers were idealized as four rods to simplify the model.

- The 4 rods were modelled with Nylon material properties

- The cards were connected to the rods via edge to surface mesh mating

- The cards were modelled with the same material properties as the structure so PEEK material with 4500 MPa of module of elasticity.

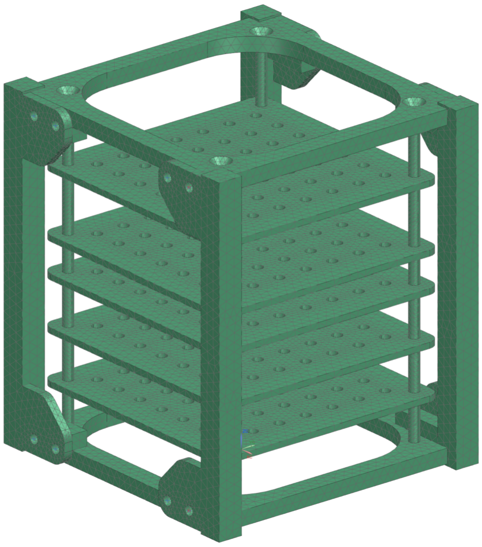

Figure 6.18: FEM Classic design with payload

Results Using this FEM models the natural frequencies were calculated:

Table 6.8: Classic design with payload FEM first 18 modes

Mode	Frequency (Hz)	Mode	Frequency (Hz)
1	264	10	492
2	274	11	501
3	288	12	583
4	290	13	618
5	356	14	619
6	400	15	633
7	452	16	713
8	462	17	799
9	474	18	808

As it can be observed from the table 6.8, in the same frequency range as the normal structure without payload, there are many more natural frequency, this is due to the presence of the 5 cards. This cards create a lot of local modes in which the structure itself doesn't move but only some of the cards do. This is more clear looking at figure 6.19

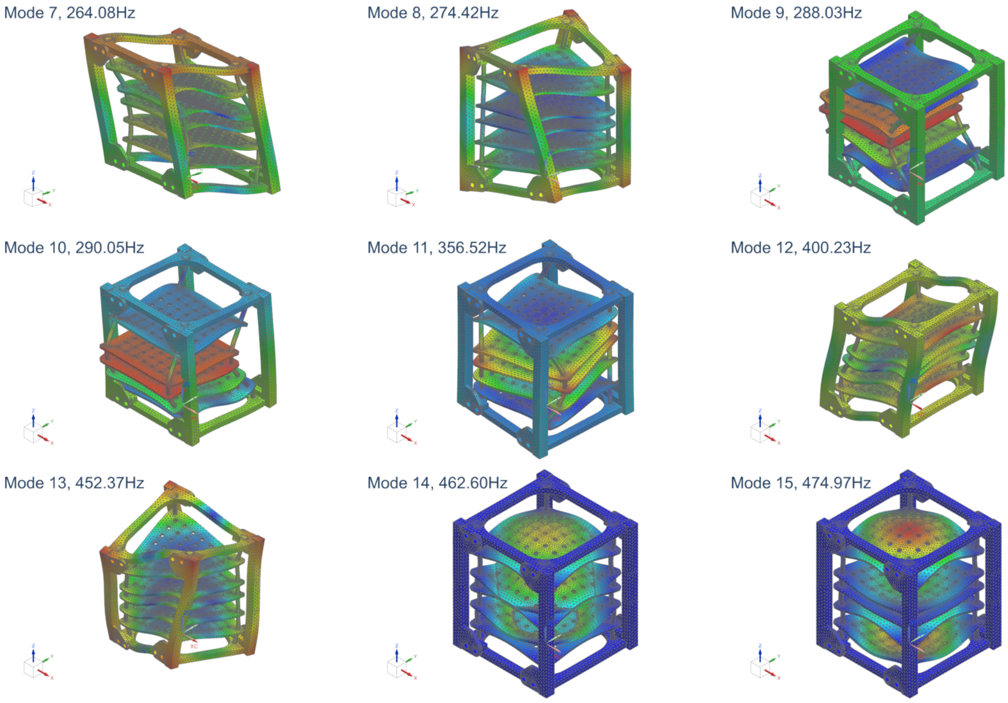

Figure 6.19: First 6 mode shapes of Classic design

6.5.2 Hammer testing

In this case only the Roving hammer approach was used following the same procedure described in the structure only case. The same hitting points were used but one was added to the top of the last plate (higher one) so that at least some mode shapes would be captured.

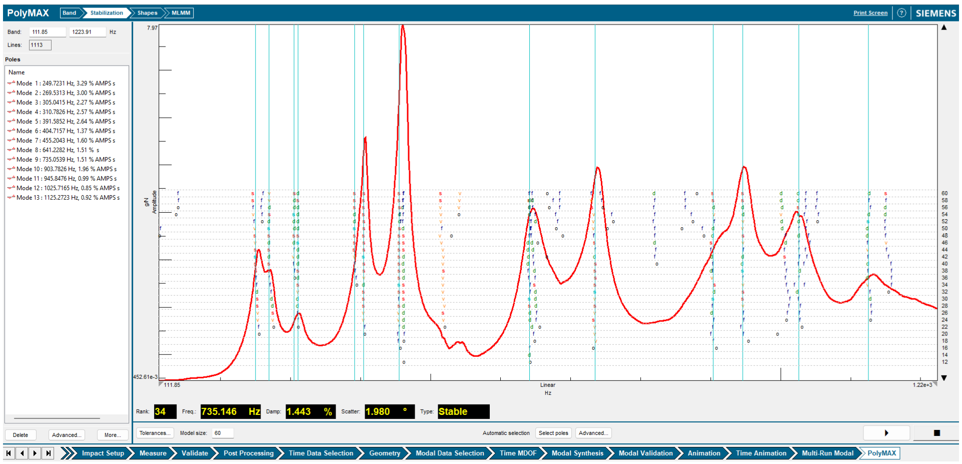

Band: 111.85 1223.91 Hz
Lines: 1113

Poles

Name
Mode 1 : 249.7231 Hz, 3.29 % AMPS s
Mode 2 : 269.5313 Hz, 3.00 % AMPS s
Mode 3 : 305.0415 Hz, 2.27 % AMPS s
Mode 4 : 310.7826 Hz, 2.57 % AMPS s
Mode 5 : 391.5852 Hz, 2.64 % AMPS s
Mode 6 : 404.7157 Hz, 1.37 % AMPS s
Mode 7 : 455.2043 Hz, 1.60 % AMPS s
Mode 8 : 641.2282 Hz, 1.51 % s
Mode 9 : 735.0539 Hz, 1.51 % AMPS s
Mode 10 : 903.7826 Hz, 1.96 % AMPS s
Mode 11 : 945.8476 Hz, 0.99 % AMPS s
Mode 12 : 1025.7165 Hz, 0.85 % AMPS s
Mode 13 : 1125.2723 Hz, 0.92 % AMPS s

Rank: 34 Freq.: 735.146 Hz Damp: 1.443 % Scatter: 1.980 ° Type: Stable

Model size: 60

Figure 6.20: Stabilization plot: roving hammer Classic design with payload

6.5.3 Correlation

Using the Classic design as structure in this case was a choice based on the correlation seen in the last section. In this case obviously the results wasn't as good as the only structure one but some observation can be made. The majority of the high MAC modes were the global modes of all the structure. The rest are the modes either of the complete stack or of the cards, looking at the figure 6.19 and in particular the modes from 3 to 5, the MAC in those cases is very low, that is because no accelerometer was put on the cards or the cards structure. Instead in figure 6.21 is possible to see a column of high MAC values, that is explained simply looking at the last two modes in figure 6.19. The top plate (the only one measured) follow the same shape as the one in the experimental case creating a high MAC in both modes but the others create different shapes.

Figure 6.21: MAC-Classic Design with payload

Table 6.9: Classic design with payload: Correlation Details

Pair	Exp. Mode	Frequency	FEM Mode	Frequency	MAC	Freq. Error (%)
1	1	249.9	1	264.1	0.877	5.69%
2	2	269.7	2	274.4	0.681	1.77%
3	6	404.8	6	400.2	0.801	-1.12%
4	7	455.3	11	501.7	0.766	10.19%
5	8	641.3	13	618.6	0.883	-3.54%
6	9	735.1	12	583.6	0.817	-20.61%
7	10	904.0	20	812.2	0.608	-10.15%
8	11	945.9	16	713.9	0.849	-24.52%
9	12	1026	17	799.2	0.842	-22.08%
10	13	1125	30	879.9	0.791	-21.81%

Chapter 7

MIMO Shaker Testing

7.1 Set-up

Now that a first Modal Analysis was completed on the structure using hammer testing technique, the next step was to recreate in the best way possible the environmental conditions that the satellite would be put through during the launch phase.
All the tests were carried out on the S.E.M.E.R.E. 4-DOF shaker system (fig. 7.1). The system is composed by 4 small conventional shakers (3 on the XY plane and 1 in the Z axis). Thanks to the positioning of the shakers the excitation Tx, Ty, and Tz can be performed but also the rotation around the z axis.
The moving plate of the shaker has a diameter of 155 mm and the maximum weight that can be put on the shaker is 2,5 kg.

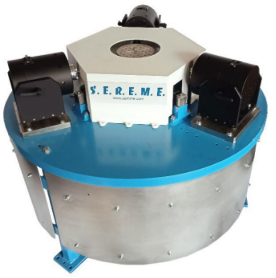

Figure 7.1: S.E.R.E.M.E. 4-DOF shaker system[xx]

7.1.1 Fixtures

One of the most important things to consider in the test definition are the boundary conditions. Theoretically a CubeSat should be tested inside his deployer but in this case is not possible. For one the deployer would weight too much already without the structure and second at this moment of the research it would be too advanced.
To test the CubeSat two different type of fixture were tested:

Realistic fixture The deployer was idealized and recreated with a simpler and lighter structure using 8xM3 threaded rods and an aluminum plate. The rods are first inserted in the table of the shaker using the M3 holes already present in the table. After that the structure would be placed in the center of the table and covered with the plate. As the plate is resting on top of the structure, 16 nuts are used to tied it into position (8 on the upper part and 8 on the under). All 16 of them are needed because if only the top one were present, the plate could flap and create noise other than create damages to the structure.

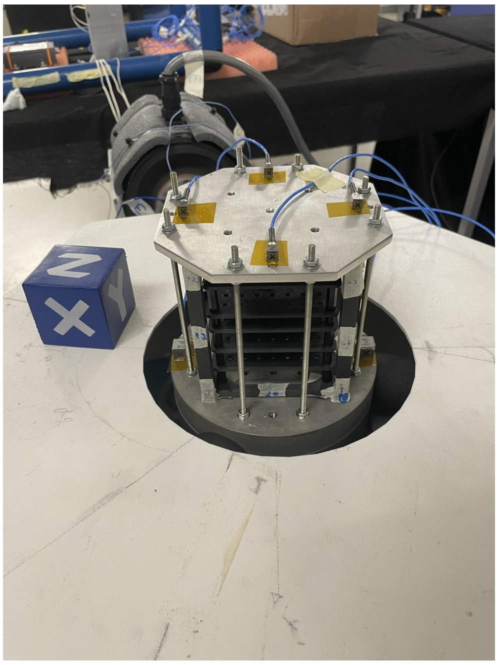

Figure 7.2: Realistic Fixture

Simplified fixture A second fixture was used to compare the results and see what were the problems in the control that would come from the realistic fixture .
In this case the CubeSat was constrained using a plate that would be inserted through the CubeSat base and block the first plate from moving.

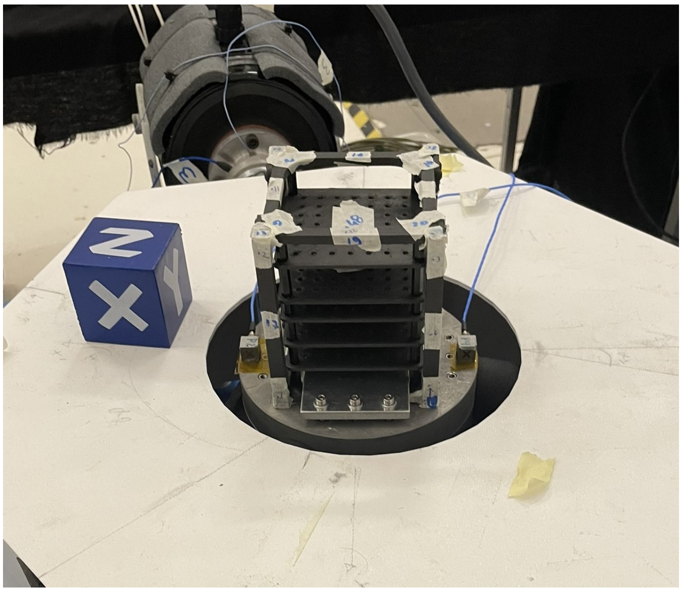

Figure 7.3: Simplified Fixture

7.1.2 Profile used

When a CubeSat needs to be launched into space it needs to pass different tests, as introduced in Chapter 3. One of this tests is the vibration tests and in particular a random control test. Each launcher has different requirements in terms of profile that needs to be applied on the structure. This profile are results of measurement of the environment in which the CubeSat will be placed during the launch. This random control tests are still conducted on one axis at a time and in some cases only positioning the spacecraft in one direction.

Using MIMO Random Control si possible to subject the spacecraft to an environment where more that one excitation is present and in different directions. In our case 4 direction, 3 translations and one rotation around the z axis.

In this part of the thesis the rotation is not going to be taken into consideration but the topic will be covered in the next chapter.

As said earlier, each launcher has its own profile. In this case the VEGA-C launcher will be used as reference. In particular, the profile of a CubeSat positioned on the SSMS Main Deck [26]. The profile is shown in figure 7.4 and the values in the table 7.1.

Table 7.1: VEGA-C Profile

Frequency Band (Hz)	PSD (10^{-3} g^2/Hz)
20 - 50	4.5
50 - 100	4.5 - 9.0
100 - 200	9.0 - 22.4
200 - 500	22.4
500 - 1000	22.4 - 5.7
1000 - 2000	5.7 - 4.5
G_{RMS}	4.4 g
Duration	60 s

The profile in our case was then scaled down to 0.89g G_{RMS} because of the limitation in terms of fixture and shaker.

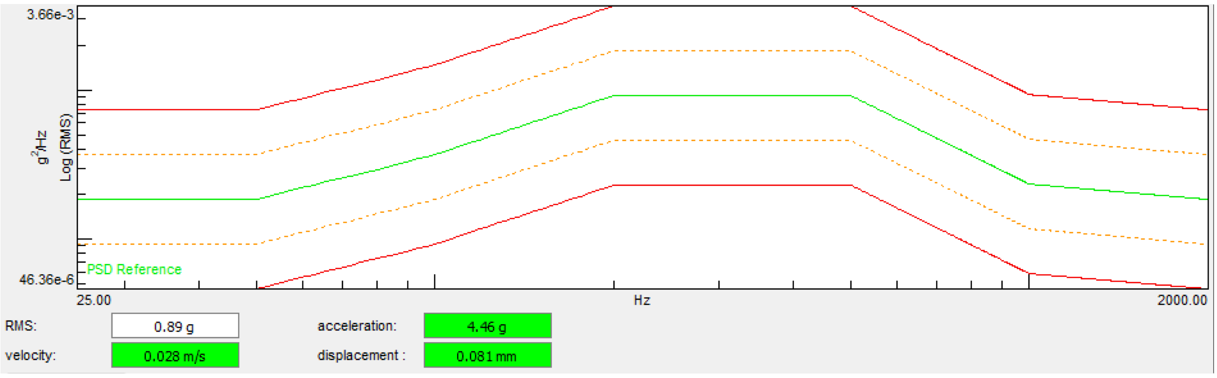

RMS: 0.89 g
velocity: 0.028 m/s
acceleration: 4.46 g
displacement : 0.081 mm

Figure 7.4: VEGA-C Profile

7.1.3 Definition of the SDM matrix

The goal of the MIMO Random Control in our case is to excite all three translations and control them. To do that the SDM matrix needed to be defined. Being a 4 DOF shaker, to be controlled 4 accelerometers need to be used. In this case 2 tri-axial accelerometers were used and of them, in particular, all three axis of the fist and the x axis of the second. In total two +X, one +Y and one +Z accelerations were used as control. The other accelerometers were used just as measure. The position of the accelerometers is shown in figure 7.5.

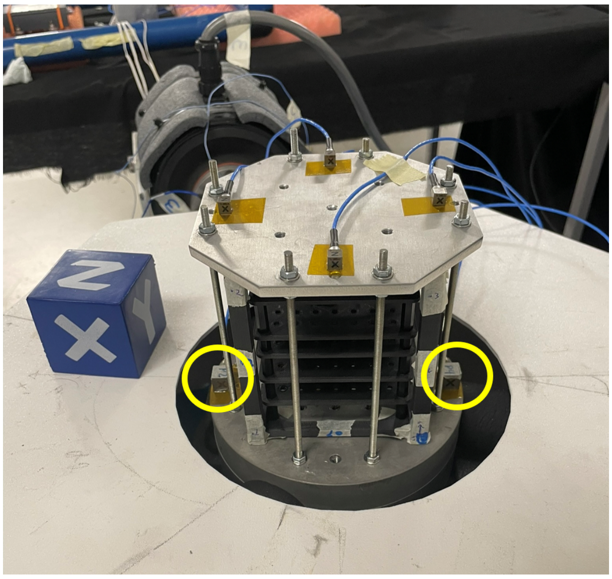

Figure 7.5: MIMO Random Setup with VEGA-C Profile

Following this geometry the SDM was created.

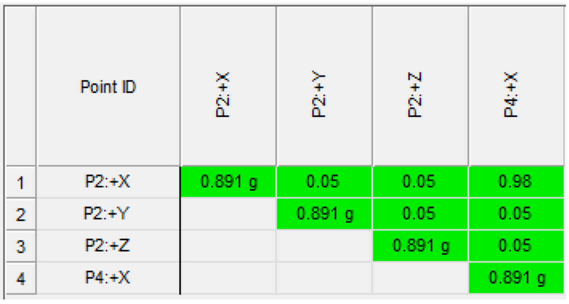

	Point ID	P2:+X	P2:+Y	P2:+Z	P4:+X
1	P2:+X	0.891 g	0.05	0.05	0.98
2	P2:+Y		0.891 g	0.05	0.05
3	P2:+Z			0.891 g	0.05
4	P4:+X				0.891 g

Figure 7.6: SDM MIMO Random Control with VEGA-C profile

As it can be observed in figure 7.6, the coherence was set to the lowest possible between the accelerometers with different direction and high coherence was set between the 2 +X accelerometers. This last part, together with the fact that 0deg of phase was set in between them was a way to impose 0 rotation around the center of the table. Using this SDM we were able to create a controlled environment depicting three uncorrelated translations.

7.2 MIMO Random Control test results

7.2.1 No limiting and 3,2 Hz resolution

The first test was conducted using the profile explained before and using a 3.2 Hz resolution.

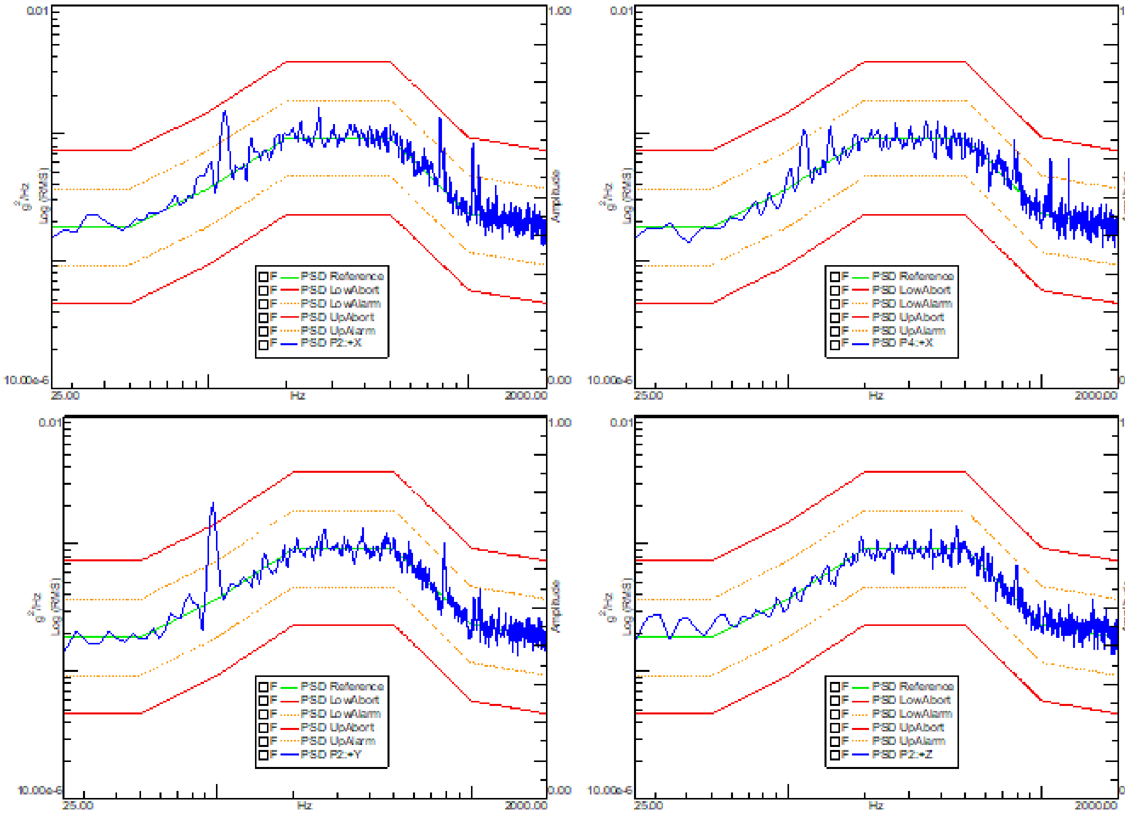

Figure 7.7: MIMO Random control with VEGA profile and 3.2 Hz frequency resolution

Figure 7.7 shows there are some peaks in the frequency range from 80 to 150 Hz but also from 700 to 900 Hz. The first peaks are being caused by the coupling between the fixture and the platform. To understand better what this means a coupling study was necessary.

7.2.2 Coupling study

Starting from the results of the MIMO Random Control test, shown in figure 7.8, is possible to see that three different peaks are present:

1. 97 Hz in the +Y direction
2. 116 Hz in the +X direction
3. 148 Hz in the +x direction

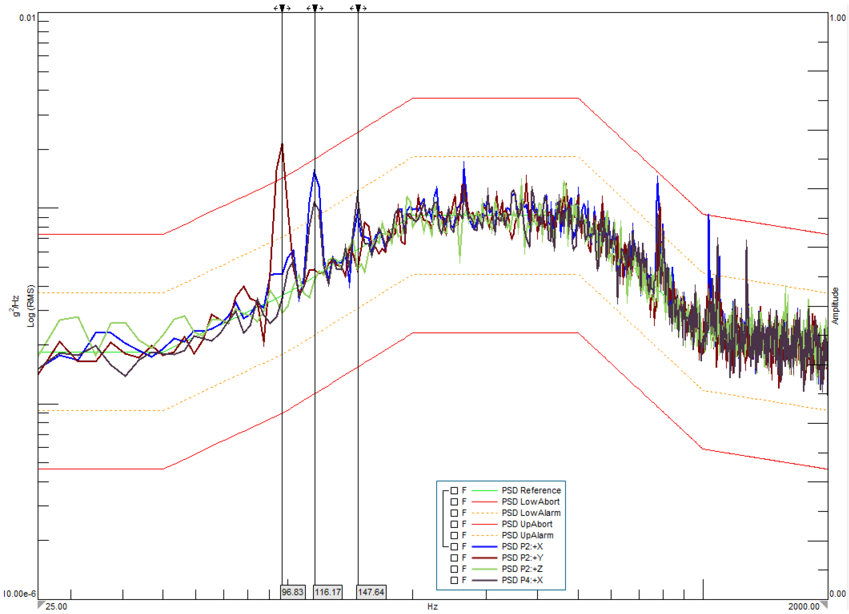

Figure 7.8: MIMO Random control diagram with all the controls

The goal of this study is to understand what is happening to the structure at those frequencies. To do that a MIMO FRF study was conducted. MIMO FRF allows the operator to do a modal analysis on a multi-DOF shaker. A more detailed instrumentation was implemented for this purpose.

Set-up To get a better understanding of the phenomenon it was important to capture the behavior of the table, the fixture and the shakers. To do that the following accelerometers combination was used:

- 3 tri-axial accelerometers are placed on the table.
- 4 tri-axial accelerometers are placed on top of the fixture.
- 4 uni-axial accelerometers are placed on the shakers to track their movement.

The geometry and SetUp are shown in figure 7.9.

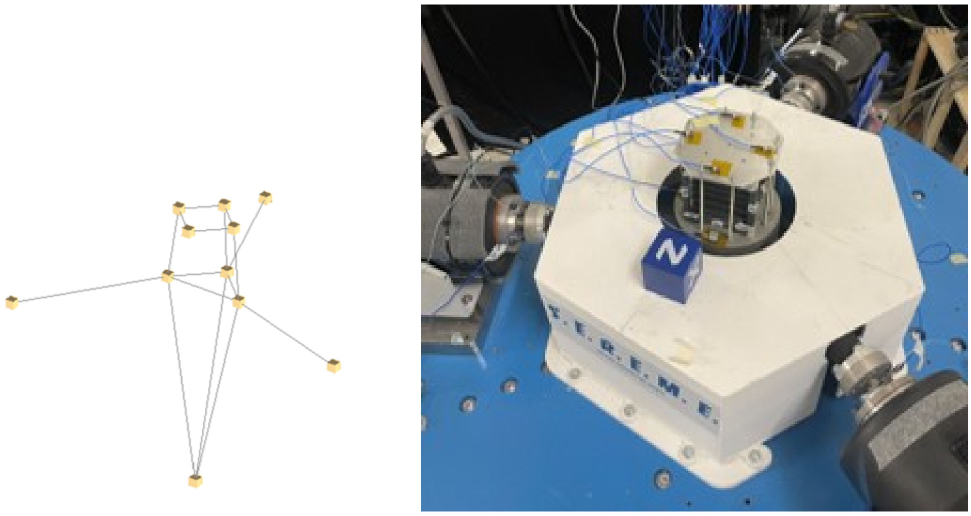

Figure 7.9: MIMO FRF geometry and SetUp

Results Using the FRFs measured from all the accelerometers it was possible to compute, using PoliMax, the stabilization diagram, figure 7.10, as in the hammer testing, and from there finding the mode shapes.

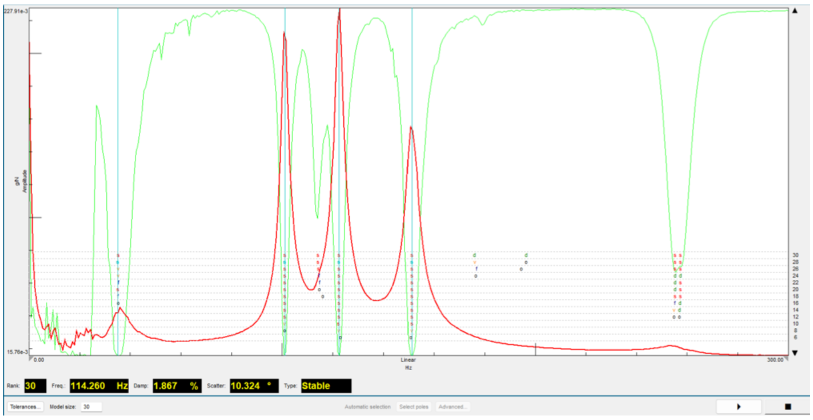

Figure 7.10: MIMO FRF stabilization diagram

Four principal modes were found and are shown in figure 7.11

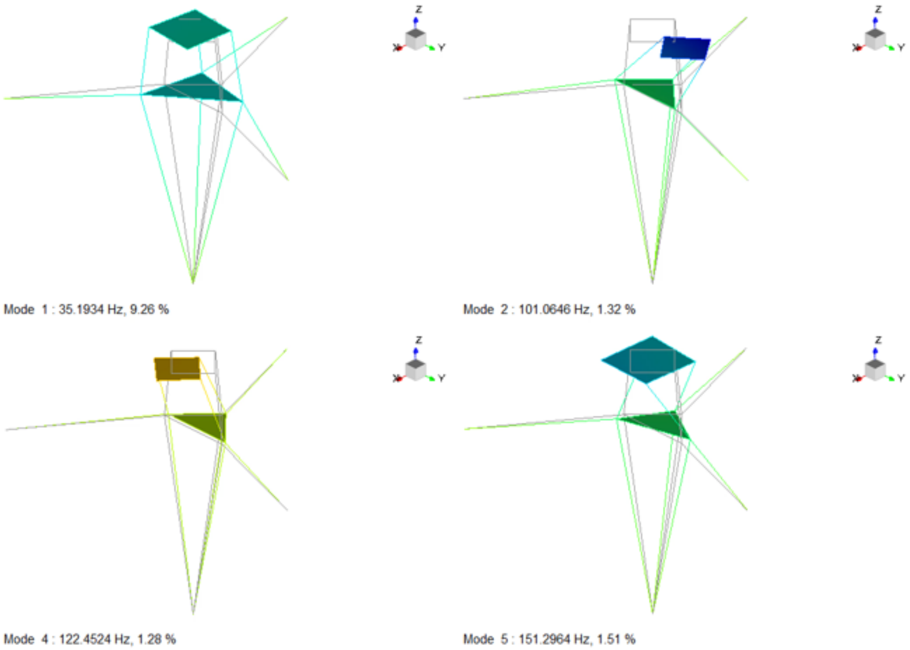

Figure 7.11: Coupling mode shapes

Table 7.2: Coupling modes frequencies

Mode	Frequency [Hz]
1	35 Hz
2	101 Hz
3	122 Hz
4	151 Hz

The frequencies found in the modal analysis (table 7.2) are the same or they are close to the ones at which the control problems occur. This gives proof that the addition of the top part of the fixture itself create problems to the control. This was expected since the high mass present at the top of the fixture and consequently the center of gravity being too high, but also because of the studs not being stiff enough on their own to contrast this modes. The modes shapes can be observed in figure 7.11. From them we can extrapolate that there is a rotation mode of the table at 35 Hz, 2 flection modes in the X and Y direction and one final torsion mode.

7.2.3 Control improvement strategies

Finer frequency resolution One strategy to tackle the problem of the coupling, is to use a finer frequency resolution. This will increase the averaging time.

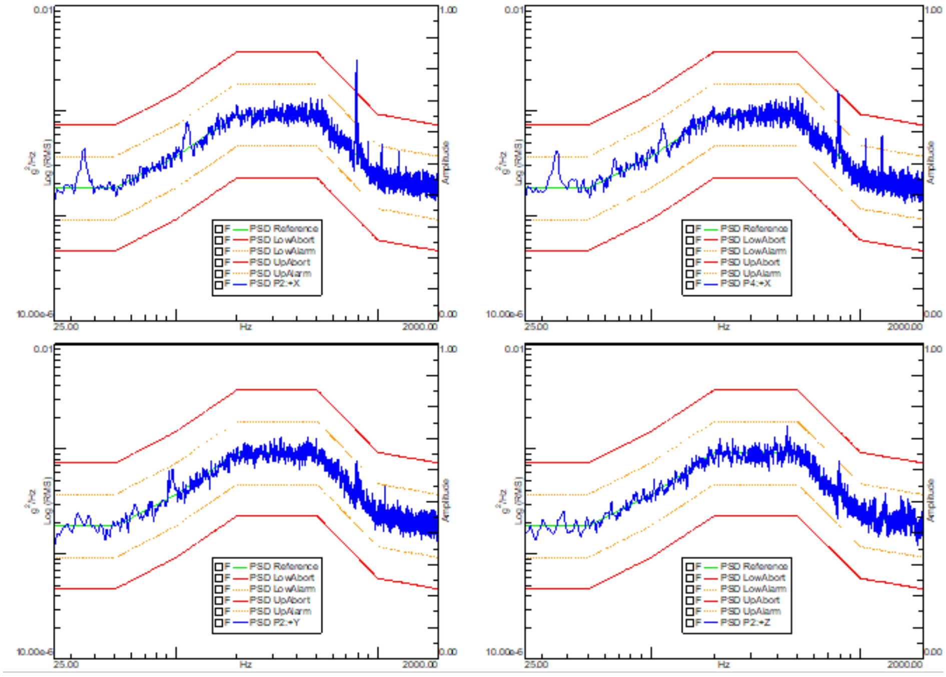

Figure 7.12: MIMO Random control with VEGA profile and 0.7 Hz frequency resolution

In figure 7.12 is possible to see that the problem at lower frequency is now less prominent and can be left as that, knowing what is the cause.
The control issue at higher frequencies is still present and important. To achieve a better result 2 types of limiting can be used:

- Force limiting
- Response limiting

Force limiting The force limiting is applied to the force cells and in particular a maximum RMS value is assigned. In this case a value of 0.3 N^2/HZ RMS was chosen after plotting the PSD of the force cells. This limit was assigned to a frequency range from 740 to 820 Hz. In this case after the limit is applied the peaks is removed so the limit is successful.

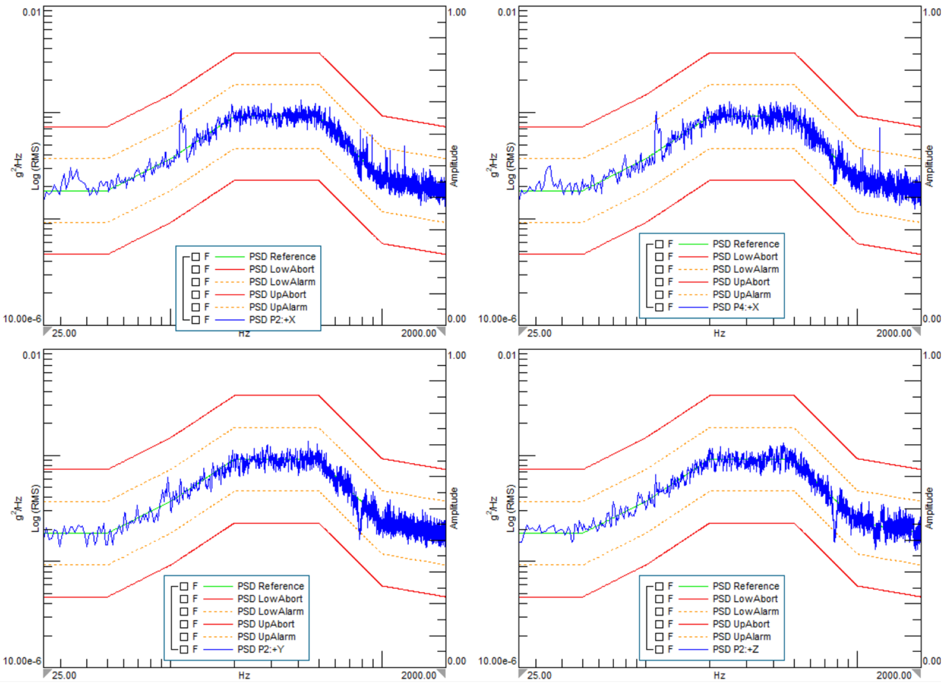

Figure 7.13: MIMO Random control with VEGA profile, 0.7 Hz frequency resolution and force limiting

Response limiting Another method is using the response limiting. This is applied to the control accelerometers and it is defined by lowering the target profile in the needed frequency range. In this case the profile was lowered by 0.25 dB in the 500-1000 Hz range.

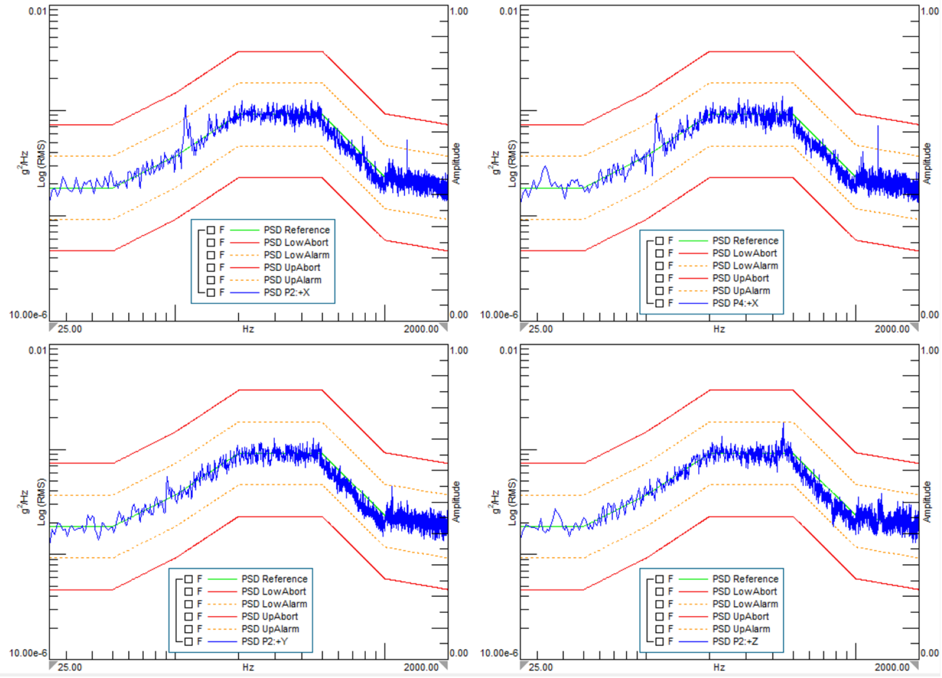

Figure 7.14: MIMO Random control with VEGA profile, 0.7 Hz frequency resolution and response limiting

Chapter 8

Replicating Rotational Responses In Multi-Axis Testing

8.1 Introduction

The previous chapter tested the structure in an environment where all three translations were present simultaneously. In this chapter, a rotation around the z-axis is introduced, this being the only rotation feasible with the test rig described earlier in Section 7.1. However, directly generating a physically meaningful rotation profile by simply applying coherence and phase relationships is not possible.
To address this, a set of signals simulating a Coupled Load Analysis (CLA) environment will be used. The data consist of time-dependent accelerations both translations and rotations recorded over a 0.6-seconds span.
The primary objective of this section is to determine a transformation matrix that can convert 6-DOF accelerations, including both translation and rotational PSD profiles, into four linear accelerations. These four accelerations form the control vector, whose PSDs serve as target profiles in the MIMO Random Control test.
Finally, using virtual channels, created from the measured data, it becomes possible to compare the recreated PSDs with the original CLA PSDs. This comparison validates whether the target environment has been successfully replicated.

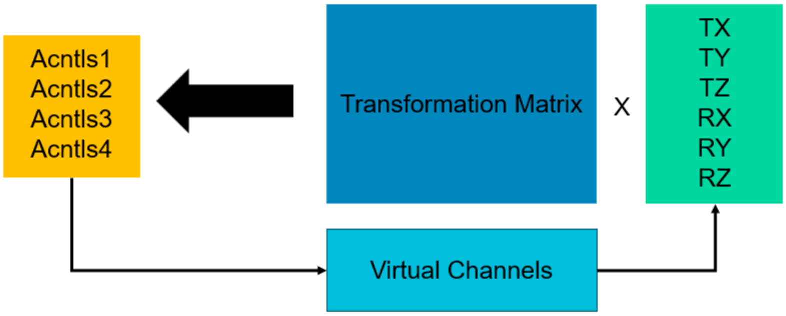

Figure 8.1: Introduction diagram

8.2 From time data to 6-DOF SDM

Before the transformation process and the testing, some signal processing was performed on the time data to have better results later on. Figure 8.2 shows an example of time signals, similar to those used in this exercise, where the first 3 DOFs have as unit of measure m/s^2 and the last 3 have rad/s^2

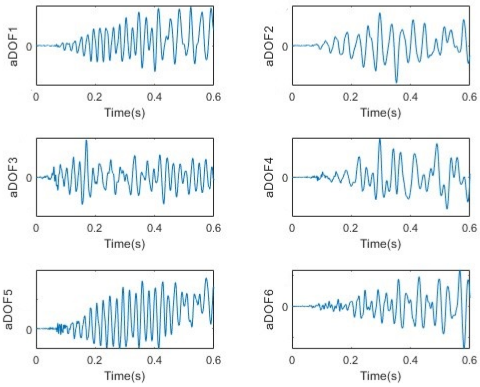

Figure 8.2: Example of time signals

The FFT (Fast Fourier Transform) of the signals are then calculated to pass from the time domain to the frequency domain. Plotting the FFTs some noise could be observed in the rotations. To eliminate this noise, a Butterworth low-pass filter with cut-off frequency of 400 Hz and order 3 was used.
After the FFTs were computed they were used to create the SDM in terms of PSDs and CSDs:

$$PSD_{ii} = FFT_i \cdot conj(FFT_i)/df$$
$$CSD_{ij} = FFT_i \cdot conj(FFT_j)/df$$

where df is frequency resolution of the data, and i and j are i-th and j-th DOF of the CLA. Both the phases and coherence are connected to the CSD value through the following formula:

$$CSD_{ij} = \sqrt{\gamma_{ij} PSD_i PSD_j} e^{i\phi_{ij}}$$

where γ_{ij} is the coherence and ϕ is the phase. The unit of measurement for the PSDs of the translations are $(m/s^2)^2/Hz$ and for the rotations $(rad/s^2)^2/Hz$.

8.3 From 6-DOF SDM to 4-DOF control SDM

The second part of this process is to perform the transformation from a 6-DOF SDM, of translations and rotation, to a 4-DOF SDM of only linear accelerations that will be the controls. To do that, a transformation matrix is required.
Starting from an equation that link a linear acceleration to a rotation acceleration is possible to write:

$$a_i(t) = a_0(t) + \alpha_0(t) \times r_i(t) \tag{8.1}$$

In vectors and matrix terms:

$$a_{DOF}(t) = T a_{ctrls}(t) \tag{8.2}$$

$$a_{ctrls}(t) = T^{\dagger} a_{DOF}(t) \tag{8.3}$$

where a_{DOF} is the vector of the accelerations of the CLA in this case and a_{ctrls} is the vector of accelerations of the controls.
They are linked by the matrix T or the inverse of it $T^{\dagger}$:

$$T^{\dagger} = \begin{bmatrix} e_1^T & (-e_1^T \times r_1) \\ \dots & \dots \\ e_N^T & (-e_N^T \times r_N) \end{bmatrix} \tag{8.4}$$

where N is the number or control accelerometers and e and r are vectors that represent respectively the versor of the accelerometer and the distance of it from the center of the table.All of this means that the transformation matrix is dependent by the sensors geometry.
In the case study that is used in this thesis the sensors geometry is the one shown in figure 8.3. The Z axis is the one exiting from the page.

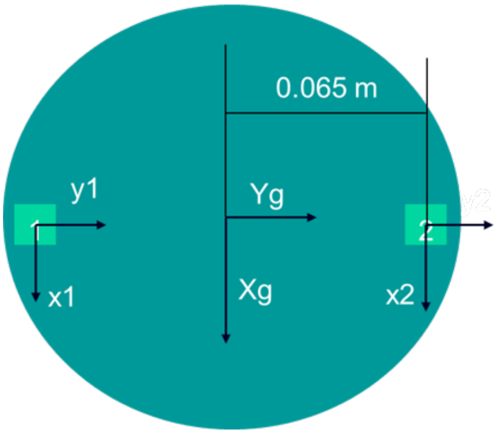

Figure 8.3: Sensors geometry

the result of this geometry is the transformation matrix in the equation 8.5.

$$T^{\dagger} = \begin{bmatrix} 1 & 0 & 0 & 0 & 0 & 0.065 \\ 0 & 1 & 0 & 0 & 0 & 0 \\ 0 & 0 & 1 & -0.065 & 0 & 0 \\ 1 & 0 & 0 & 0 & 0 & -0.065 \end{bmatrix} \tag{8.5}$$

The transformation matrix is then used to transform the SDM matrix:

$$S_{ctrls}^{ref} = T^{\dagger} \quad S_{DOF}^{ref} \quad (T^{\dagger})' \tag{8.6}$$

The S_{ctrls}^{ref} is now a 4x4 matrix.
After the 4-DOF matrix is computed, it can be exported to TestLab and used as reference matrix in the MIMO Random Control module (figure 8.4).

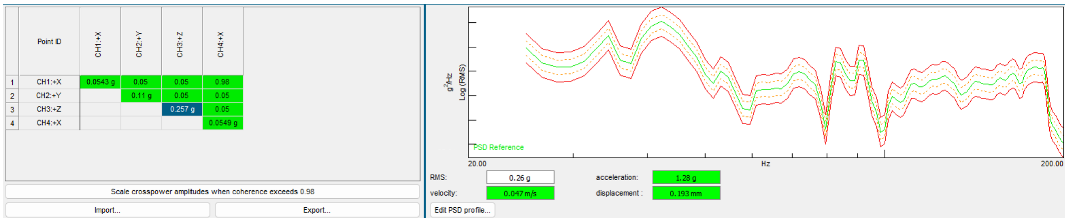

	Point ID	CH1:+X	CH2:+Y	CH3:+Z	CH4:+X
1	CH1:+X	0.0543 g	0.05	0.05	0.98
2	CH2:+Y		0.11 g	0.05	0.05
3	CH3:+Z			0.257 g	0.05
4	CH4:+X				0.0549 g

Scale crosspower amplitudes when coherence exceeds 0.98

RMS: 0.26 g
acceleration: 1.28 g
velocity: 0.047 m/s
displacement : 0.193 mm

Figure 8.4: TestLab SDM

8.4 Tests

8.4.1 Virtual channel creation

Before running the tests, the virtual channel needs to be created. When looking a the equation 8.2, now the a_{DOF} are known, because they are the one measured by the accelerometers, so it is possible to find back the time acceleration simply multiplying them by the matrix T. T is the inverse of the matrix shown in equation 8.5. In particular, for this case:

$$\begin{Bmatrix} Tx \\ Ty \\ Tz \\ Rx \\ Ry \\ Rz \end{Bmatrix} = \begin{bmatrix} 0.5 & 0 & 0 & 0.5 \\ 0 & 1 & 0 & 0 \\ 0 & 0 & 1 & 0 \\ 0 & 0 & 0 & 0 \\ 0 & 0 & 0 & 0 \\ 7.63 & 0 & 0 & -7.63 \end{bmatrix} \begin{Bmatrix} a_{1x} \\ a_{1y} \\ a_{1z} \\ a_{2x} \end{Bmatrix} \tag{8.7}$$

The final virtual channel equation that are going to be put in the channel setup are going to be:

$$Tx = (a_{1x} + a_{2x})/2 \tag{8.8}$$

$$Rz = (7.63 \cdot a_{1x} - 7.63 \cdot a_{2x}) \cdot 9.81 \tag{8.9}$$

The translation Tx is an average of the 2 translational accelerations along the +X axis, the other two translations are controlled directly by the respective accelerometers and the only rotation possible as anticipated before is the Rz that is going to be a subtraction of the rotation accelerations of the two channels. Inside the parenthesis the units are g/m because the coefficient 7.63 is actually the inverse of the distance so it has a unit of 1/m. After the parenthesis to have a rad/s^2 unit, the parenthesis needs to be multiplied by 9.81 m/s^2.

8.4.2 Results

After the virtual channel were created, a MIMO Random control test with 0.39 Hz resolution and frequency range from 25 to 200 Hz was launched using the SDM shown in figure 8.4. The range was defined following the fact that, after 200 Hz, the PSDs are very low in values. The results in terms of control are shown in figure 8.5.

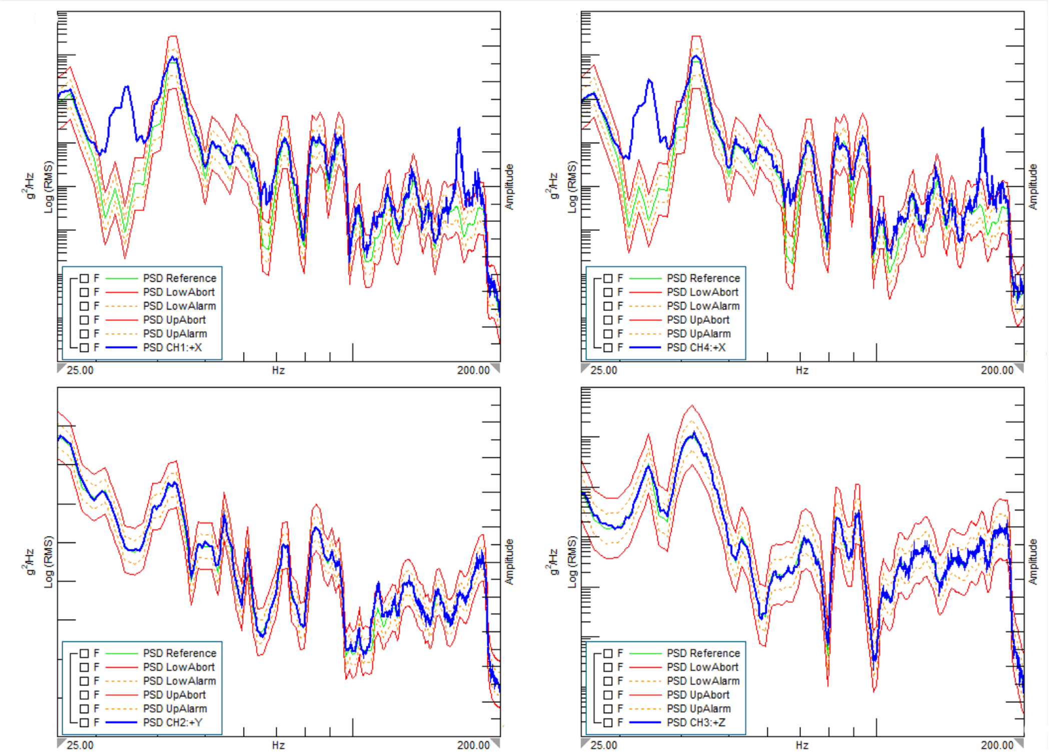

Figure 8.5: Control PSDs

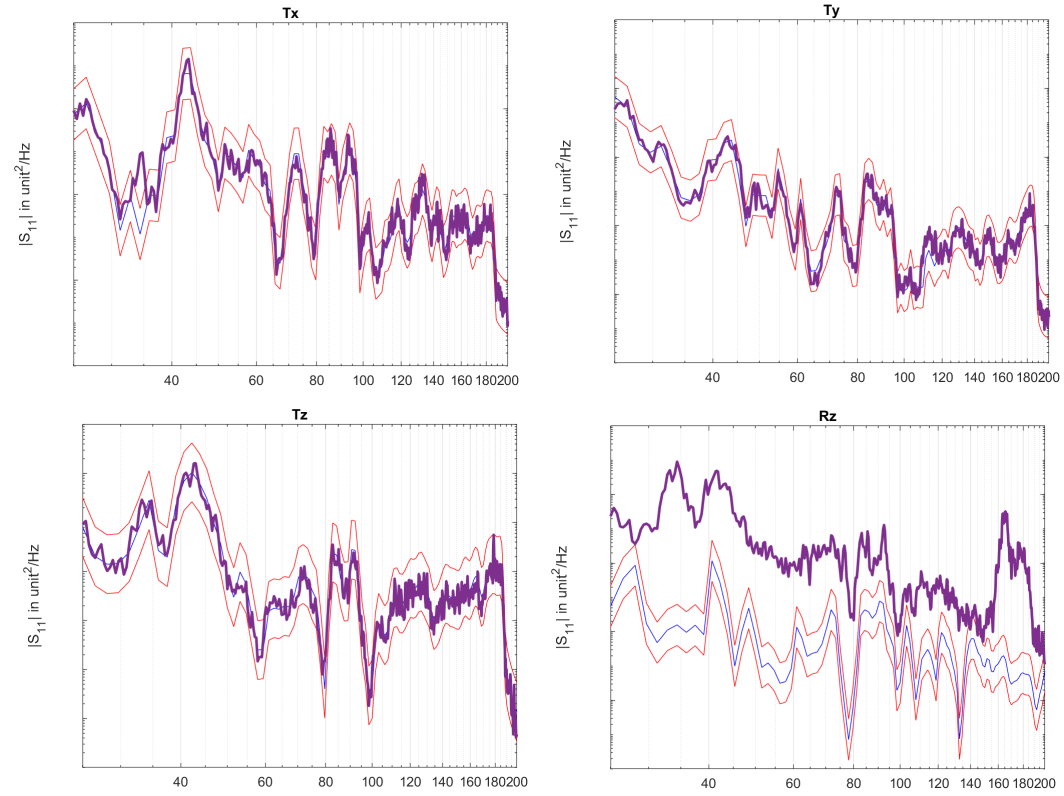

Figure 8.6: Measured PSDs (purple) compared to the original ones (blu line)

In terms of control PSDs the results are fairly good, with the exception of a couple of frequency ranges. The first peak which is out of the controls is caused by the rotation

mode of the table which is the same found in the coupling study.
More important are the results in terms of comparison between the measured ones and the initial 6-DOF PSDs. This is shown in figure 8.6.

The translations are accurately represented, remaining within the ±6 dB range of the target PSDs for most of the frequency range.
The rotation, however, exceeds the target significantly. This occurs because the required rotation is nearly zero, making it negligible compared to the translations. To recreate the translation environment, the table inadvertently induces a small rotation, which ends up being larger than the target value.
The minimal magnitude of the rotation is also evident from the phase relationship between the two +X control PSDs, as shown in the bottom-left corner of figure **??**, where the phase is nearly zero.

8.4.3 Upping the rotation

One way of validating the work that has been done still using the data from the time signals is by multiplying the rotation Rz, at the beginning when is still in the time domain, by a factor of 50.
By doing that the 6-DOF will change only in the terms that use that rotation.
The biggest changes arise when the 4-DOF control SDM is computed. The modifications in the original SDm leads to changes in the PSD profiles of the +X controls that dictate the rotation.
The same tests were ran again with this last control SDM. The control results are shown in figure 8.7.

The results are similar to the one before, the Y and Z controls are perfect and in the

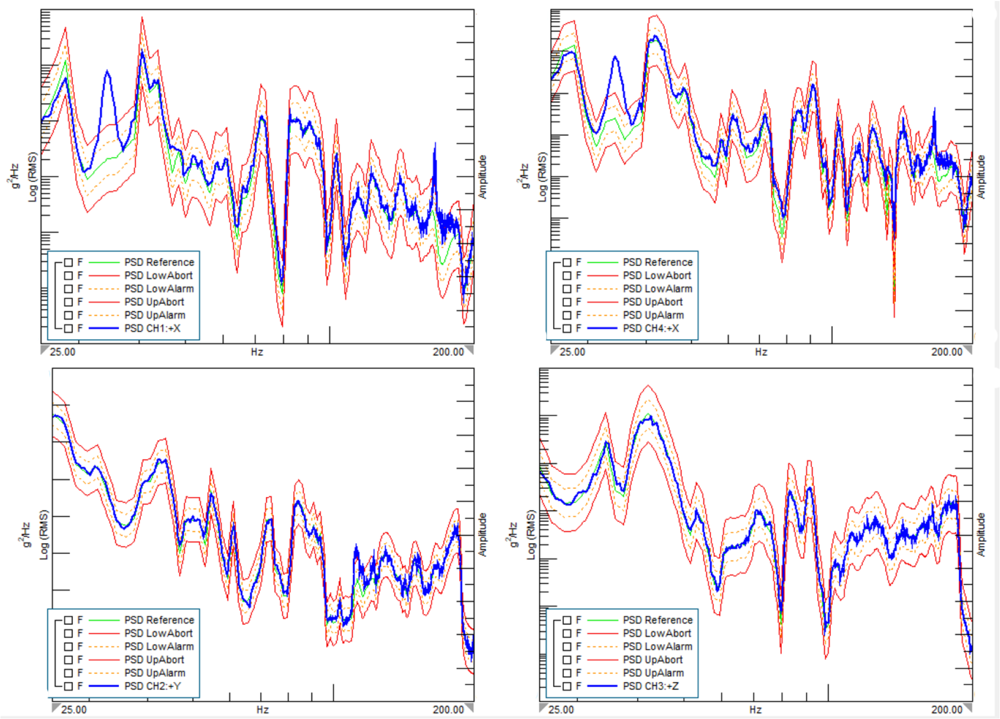

Figure 8.7: Control PSDs when upping the rotations

+Xs only in the frequencies where there is a coupling mode there are some issues.
The difference is present when the measured PSDs are compared to the CLA ones

(figure 8.8).

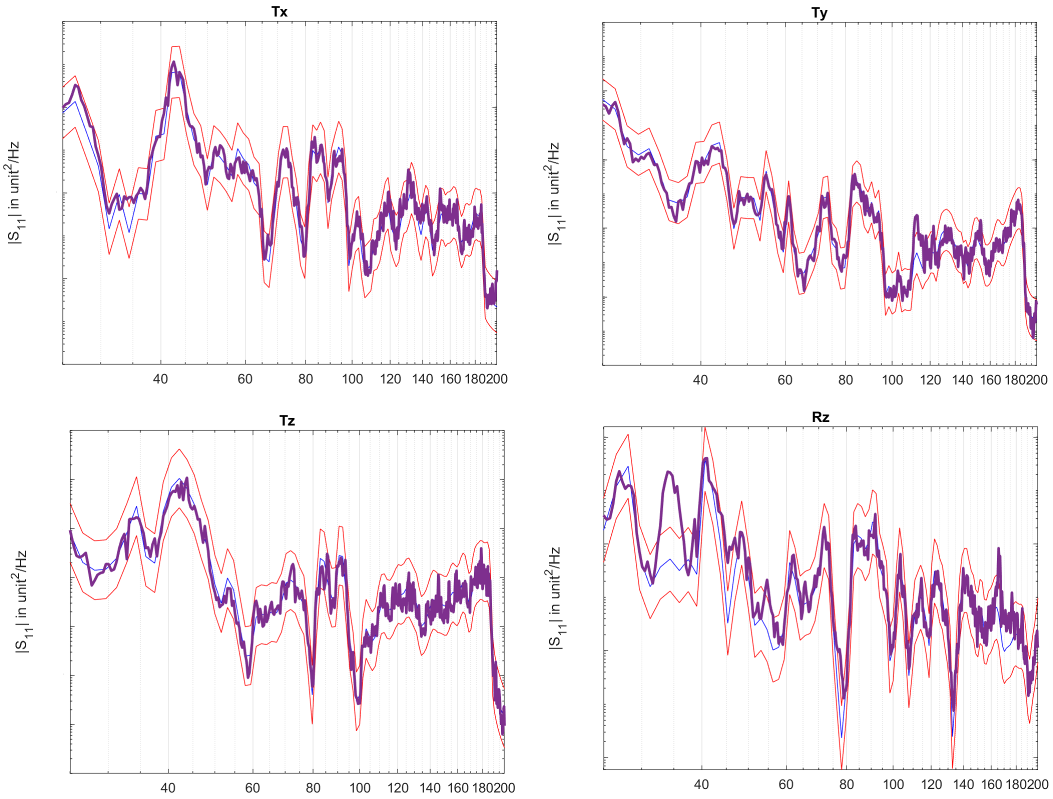

Figure 8.8: Measured PSDs (purple) compared to the original ones (blu line) after upping the rotation

Now looking at figure 8.8, even the rotation is controlled, apart from the same frequency range as the control issues, which was the goal of this chapter.

Chapter 9

Conclusions

This work provides a comprehensive overview of the initial stages of a CubeSat life cycle. It began with the design process, adhering to CubeSat standard regulations. The focus then shifted to additive manufacturing using PEEK, one of the most advanced materials in the field. The manufacturing process was successful, yielding components with precise dimensions and appealing aesthetics, demonstrating that robust structural integrity can be achieved using this method.

Following manufacturing, an initial modal analysis was performed. This analysis highlighted the importance of improving the material model by moving beyond the isotropic material approximation used in this study. Despite this simplification, the modal analysis revealed good mode shape correlations in the classic CubeSat structural design.

Next, MIMO Random Control shaker tests were conducted on a 4-DOF shaker platform, using a scaled-down qualification profile from VEGA-C. The shaker's capabilities allowed simultaneous excitation of all translational axes, creating a realistic test environment. These tests evaluated the controllability of the structure with various fixture solutions. Among these, the most realistic fixture, due to its mass and center of gravity position, proved the most challenging to control. The fixture's modes interfered with achieving perfect control. To better understand these modes, a MIMO FRF test was conducted, which provided deeper insights into their shapes and frequencies. For heavier tests on this structure, an alternative fixture, such as the simplified one proposed in this thesis, would be necessary.

The final phase of this study aimed to replicate a Coupled Load Analysis (CLA) -like environment on the same platform. A script and methodology were developed using an algebraic approach to transform an environment characterized by translations and rotations into one defined solely by linear accelerations for control purposes. The results met expectations, with the four CLA-like DOFs of interest (Tx, Ty, Tz, and Rz) accurately recreated. A comparison with the initial data confirmed the validity of the process and the scripts employed.

This thesis opens up opportunities for further testing using other types of signals on similar structures, paving the way for a deeper understanding of their usability in real space environments.

Bibliography

[1] CubeSat Design Specification Rev. 14.1.The CubeSat Program, Cal Poly SLO.

[2] `https://en.wikipedia.org/wiki/NCube_(satellites)`.

[3] `https://www.cubesatshop.com/product/3-unit-cubesat-deployer/`.

[4] NASA/TP—2024–10001462. State-of-the-Art. Small Spacecraft Technology. Small Spacecraft Systems Virtual Institute. Ames Research Center, Moffett Field, California .ù

[5] `https://www.endurosat.com/products/1u-cubesat-structure/`.

[6] Simon Ford, Mélanie Despeisse, Additive manufacturing and sustainability: an exploratory study of the advantages and challenges, Journal of Cleaner Production.Volume 137.2016. Pages 1573-1587. ISSN 0959-6526. `https://doi.org/10.1016/j.jclepro.2016.04.150.`.

[7] Ala'aldin Alafaghani, Ala Qattawi, Buraaq Alrawi, Arturo Guzman, Experimental Optimization of Fused Deposition Modelling Processing Parameters: A Design-for-Manufacturing Approach. Procedia Manufacturing. Volume 10. 2017. Pages 791-803. ISSN 2351-9789.

[8] 3D Printed Satellite Metal Component Built by Thales Alenia Space and Poly-Shape with Concept Laser AM Technology. https://www.voxelmatters.com/3d-printed-satellite-metal-component-built-by-thales-alenia-space-and-poly-shape-with-concept-laser-am-technology/.

[9] Y. Kwon, L. Brewer, R. Panholzer, D. Sakoda, C. Park, "Direct Manufacturing of CubeSat Using 3-D Digital Printer and Determination of Its Mechanical Properties" Naval Postgraduate School, Monterey, CA.

[10] Napoli, Matthew. The Use of Additive Manufacturing Technologies for the Design and Development of a Cubesat. Diss. San Josè University, 2013.

[11] Rinaldi, M.; Cecchini, F.; Pigliaru, L.; Ghidini, T.; Lumaca, F.; Nanni, F. Additive Manufacturing of Polyether Ether Ketone (PEEK) for Space Applications: A Nanosat Polymeric Structure. Polymers 2021, 13, 11. `https://doi.org/10.3390/polym13010011`.

[12] Hapuhennedige Sachith Warnakulasuriya. Vibration Analysis and Testing of a Satellite Structure during its Launch and In-flight Stages.

[13] Singiresu S. Rao. Mechanical Vibrations- 2004. Upper Saddle River: Pearson-Prentice Hall, 1993.

[14] Alfonso Pagani. Slides corso di Strutture Aerospaziali.

[15] https://community.sw.siemens.com/s/article/what-is-a-frequency-response-function-frf.

[16] Ward Heylen, Stefan Lammens, Paul Sas. Modal Analysis Theory and Testing.

[17] https://community.sw.siemens.com/s/article/simcenter-testlab-impact-testing.

[18] United states standard 810 G. Method 527.1 multi-exciter test. Oct 2008.

[19] J. S. Bendat and A. G. Piersol. Random Data: Analysis and Mea- surement Procedures, 4th Edition. Ed. by Wiley. Mar. 2010.

[20] U. Musella, G. D'Elia, S. Manzato, B. Peeters, F. Marulo P. Guil- laume, and E. Mucchi. "Tackling the target matrix definition in MIMO Random Vibration Control testing". In: XXX Aerospace Testing Seminar (Mar. 2017).

[21] G. H. Golub and C. van Loan. Matrix Computation. Ed. by The Johns Hopkins University Press. 1996.

[22] C. D. Meyer. Matrix analysis and applied linear algebra. Ed. by Society for Industrial and Applied Mathematics. 2000.

[23] `https://markforged.com/materials/plastics/onyx-esd`.

[24] `https://s3.amazonaws.com/mf.product.doc.images/Datasheets/Translations/IT/Markforged_CompositesV5.1_it.pdf`.

[25] https://www.roboze.com/it/risorse/stampa-3d-del-peek-cos-e-il-peek-e-a-cosa-serve.html.

[26] Small Spacecraft Mission Service VEGA-C. User's manual Issue 1 - Revision 0. Sept. 2020. arianspace. `https://ariane.group/app/uploads/sites/4/2024/10/SSMS-Vega-C-UsersManual-Issue-1-Rev0-Sept2020.pdf`